Advanced Theory and Simulations

ADVANCED THEORY AND SIMULATIONS
www.advtheorysimul.com

RESEARCH ARTICLE

Performance Engineering of Cs_2AuScI_6 Double Halide Perovskite Solar Cell: A DFT and SCAPS-1D Approach to 31.82% Efficiency

Shuaib Mahmud[1,2] | Md. Mainol Islam[1] | Md. Mukter Hossain[2] | Md. Mohi Uddin[2] | Md. Ashraf Ali[2]

[1]Department of Electrical and Electronic Engineering, Jatiya Kabi Kazi Nazrul Islam University (JKKNIU), Mymensingh-2224, Bangladesh | [2]Advanced Computational Materials Research Laboratory, Department of Physics, Chittagong University of Engineering and Technology (CUET), Chattogram, Bangladesh

Correspondence: Shuaib Mahmud (shuaibmahmud@jkkniu.edu.bd) | Md. Ashraf Ali (ashrafphy31@cuet.ac.bd)

Received: 3 September 2025 | **Revised:** 5 November 2025 | **Accepted:** 18 November 2025

Keywords: DFT | double halide perovskite | SCAPS-1D | semiconductor | solar cell

ABSTRACT

In response to pressing environmental priorities, the development of nontoxic and stable alternatives to lead-based Perovskite solar cells is critical. This study focuses on Cs_2AuScI_6, a lead-free Perovskite, as a promising photovoltaic material. Through density functional theory (DFT) calculations using Wien2k, a bandgap of 1.30 eV is revealed, with Au-*d* and Sc-*d* orbitals playing key roles in electronic properties and Au atoms dominating charge distribution. The material exhibits visible absorption peaks of the 10^5 order, indicating its potential for solar applications. Conducted by DFT, 36 configurations combining various electron transport layers and hole transport layers (HTLs) are investigated. Copper Barium Tin Sulfide (CBTS) is identified as the optimal HTL due to its alignment with the absorber material. Five standout device architectures of ITO/WS_2/Cs_2AuScI_6/CBTS/Ni, ITO/ZnO/Cs_2AuScI_6/CBTS/Ni, ITO/TiO_2/Cs_2AuScI_6/CBTS/Ni, ITO/PCBM/Cs_2AuScI_6/CBTS/Ni, and ITO/IGZO/Cs_2AuScI_6/CBTS/Ni (Where ITO means Indium Tin Oxide) achieved exceptional power conversion efficiencies of 31.48%, 31.46%, 29.44%, 28.75%, and 31.82%, respectively, surpassing the 18.61% efficiency of the ITO/C_{60}/Cs_2AuScI_6/CBTS/Ni structure. The study further examines practical performance factors, including resistances, temperature effects, current–voltage (*J*–*V*) characteristics, and quantum efficiency, thereby enhancing its real-world applicability. These findings highlight the potential of Cs_2AuScI_6 as a nontoxic, inorganic alternative for perovskite solar technology, contributing to the sustainable development of photovoltaics.

1 | Introduction

The growing global energy demand from the rising population, rapid urbanization, and the expansion of industries highlights the need for sustainable energy solutions [1]. Fossil fuels, which are inherently finite, substantially contribute to environmental deterioration, including greenhouse gas emissions and climate change [2–3]. Solar energy, especially perovskite solar cells (PSCs), offers a clean, efficient, and cost-effective alternative energy source that is versatile and suitable for many applications [4]. Perovskite materials have transformed the photovoltaics sector due to their superior optoelectronic characteristics. The general formula of perovskite is ABX_3, characterized by high absorption coefficients, adjustable bandgaps, and superior charge carrier mobility. The characteristics of these features have enabled PSCs to attain power conversion efficiencies (PCEs) that are equivalent to, or even exceed, those of conventional silicon-based technology. The capacity for low-temperature processing

using solution techniques enhances the cost-effectiveness and manufacturability of these cells. Nonetheless, the use of lead-based perovskites has been associated with environmental and health hazards stemming from lead poisoning [5]. The release of lead during the operation or disposal of the cells is a risk that cannot be ignored. Therefore, the focus has been moved to lead-free alternatives that exhibit efficient photovoltaic properties and are sustainable.

Double perovskite materials, with their exceptional chemical and physical properties, have driven research and development in many technological and industrial sectors [6–9]. In lead-free double perovskites, their excellent optoelectronic performance and high solar spectrum absorption have enabled power conversion efficiencies [10]. They have thus driven efforts toward such integration in energy applications, particularly in photovoltaic (PV) devices [11]. Double perovskites have greater chemical diversity than their single perovskite counterparts, which have a general formula $A_2B'B''X_6$. A in the structure of the complexes represents a large metal cation (e.g., Cs^{1+}), B' and B'' are smaller metal cations, and X is an anion (most commonly halides or oxides)[12]. In the 1960s, double perovskites were first synthesized and found to be chemically stable and less toxic, leading to interest in their energy-related applications [13–14]. Hybrid organic–inorganic halide perovskites, such as $CH_3NH_3PbI_3$ have demonstrated PCE over 22% [15], making them a potential competitive replacement for silicon-based solar cells. Despite this, the development of lead-free double perovskites has been hastened by concerns regarding lead toxicity.

Halide-based double perovskites have attracted significant interest as optoelectronic and photovoltaic materials due to their direct/indirect bandgaps, high absorption coefficients, and excellent charge carrier mobilities [16–19]. Among them, $Cs_2AgBiBr_6$ has been extensively studied, exhibiting tunable bandgaps of 1.61, 1.654, and ∼2 eV, with notable photovoltaic performances of 26.3%, 23.5%, and 25.2%, by different researcher respectively [20–22]. Meng et al. [11] explored $Cs_2InBiBr_6$ as an absorber, achieving a PCE of 23.64% with a direct bandgap of 1.27 eV, using TiO_2 as the electron transport layer (ETL) and Cu_2O as the hole transport layer (HTL). Utsho et al. [23] achieved a power conversion efficiency (PCE) of 19.70% using the device architecture ITO/WS_2/$Cs_2CuBiBr_6$/CBTS/Ni, with an absorber bandgap of 1.24 eV. Similarly, Kale et al. [24] investigated the Au-based absorber $Cs_2AuBiCl_6$, reporting a bandgap of 1.40 eV (close to the Shockley–Queisser limit) and a PCE of 22.18%. Besides, Arfaoui et al. explored $CsGeI_3$/$FASnI_3$, $FASnI_3$/$FAGeCl_3$, $FASnI_3$, and MAGeI3/$FASnI_3$ tandem based PSC, achieving a PCE of 30.42%, 30%, 28.13%, and 25.69%; demonstrating the impact of bandgap tuning on device performance and emphasizing the feasibility of simplified and eco-friendly perovskite architecture [25–28]. Together with density functional theory (DFT) and experimental studies on $Cs_2AgBiBr_6$ and Rb_2AgBiI_6, the findings indicate that these materials are promising solar absorbers with an ideal bandgap (1.98 eV) and excellent ambient stability [29–30]. The potential applications highlighted in previous literature inspired us to explore double perovskite halides. Therefore, we aimed to identify promising double perovskite halides for renewable or solar energy applications.

The architecture of a solar cell is very important with regard to the charge carrier dynamics and efficiency of the cell. To our knowledge, no study has explored the PCE of photovoltaic devices using Cs_2AuScI_6 as the absorber layer. In this work, the proposed device configuration is ITO/ETL/Cs_2AuScI_6/ HTL/Ni, where the absorber layer is Cs_2AuScI_6. ITO and nickel (Ni) are used as transparent conductive electrodes and back contacts, respectively. The above-mentioned structure is a planar heterojunction design known for its simplicity and scalability. The transport properties of ETLs and HTLs in enhancing device performance are also investigated. Six ETLs (WS_2, ZnO, TiO_2, PCBM, IGZO, C_{60}) and six HTLs [CBTS, CdTe, P_3HT, PEDOT:PSS (Poly 3,4 ethylene dioxythiophene:Polystyrene sulfonate), PTAA (Poly Triarylamine), CuI] are examined. These materials have been selected due to their unique electronic properties and compatibility with Cs_2AuScI_6.

Traditional **ETLs**, such as **TiO_2** and **ZnO**, ensure effective electron extraction but suffer from drawbacks including high-temperature processing, UV-induced degradation, and interfacial instability. Fullerene-based ETLs like **PCBM** and **C_{60}** offer smooth interfaces and good energy alignment yet face cost and stability issues. Emerging materials such as **WS_2** and **IGZO** show promise due to their high electron mobility, chemical robustness, and low-temperature processability. Similarly, common **HTLs** like **PEDOT:PSS** and **P_3HT** provide good conductivity but are limited by instability and poor charge transport. Inorganic HTLs such as **CuI**, **CBTS**, and **CdTe** exhibit better stability, though CdTe's toxicity and processing demands remain concerns, while **PTAA** offers high mobility but is costly. These limitations highlight the urgent need for new HTL and ETL materials combining stability, ideal energy-level alignment, and low-cost fabrication to enable highly efficient and durable photovoltaic devices.

This work investigates the application of the lead-free Cs_2AuScI_6 double halide perovskite material for solar cells by exploring its structural, electronic, and optical properties using DFT simulations within the Solar Cell Capacitance Simulator-1Dimensional (SCAPS-1D) model. The focus is on developing new, environmentally friendly, and cost-efficient materials for future renewable energy technologies. The efficacy of Cs_2AuScI_6 solar cells was enhanced with the judicious selection of hole transport layer and electron transport layer components. Following the selection of optimal material combinations, the influence of the Cs_2AuScI_6 absorber and electron transport layer (ETL) thickness on critical performance indicators, including open-circuit voltage (V_{OC}), short-circuit current density (J_{SC}), fill factor (FF), and power conversion efficiency (PCE) was assessed. This study also examines the impacts of resistance (both series and shunt), temperature, capacitance, Mott–Schottky (MS) behavior, generation and recombination rates, current–voltage (J–V) characteristics, and quantum efficiency (QE). This study presents a comprehensive framework for designing high-efficiency, lead-free perovskite solar cells by integrating DFT with SCAPS-1D simulations, offering valuable insights for advancing sustainable photovoltaic technologies and addressing the pressing issue of lead toxicity in perovskites. The results aim to facilitate future progress in efficient and eco-friendly solar energy conversion.

2 | Methodology

2.1 | Wien2k

DFT computations were performed in this work using the Wien2k code [31], which resolves the Kohn–Sham equation. The generalized gradient approximation (GGA) using the Perdew–Burke–Ernzerhof (PBE) functional was used to ascertain ground state characteristics [32]. The full potential LAPW (Linearized Augmented Plane Wave) approach was employed for structural optimization, utilizing the third-order Birch–Murnaghan equation of state. The initialization procedure included essential parameters: This encompasses a bond length factor of 3, an energy gap of −6.0 Ry between valence and core states, an $R_{MT}\times K_{MAX}$ value of 7, a k-point grid of 1000 ($10\times10\times10$), and a G_{MAX} value of 12. Electronic wave functions were updated via the self-consistent field (SCF) calculations to solve the Kohn–Sham equations iteratively, and the charge density was iteratively repeated until convergence. Energy and charge convergence thresholds were set to 0.0001 Ry and 0.0001 e, respectively. Finally, to enhance accuracy in optoelectronic property predictions, the Tran–Blaha modified Becke–Johnson (TB–mBJ) potential was applied [33], which is between precision and computational efficiency for inorganic materials.

2.2 | SCAPS-1D Numerical Simulation

The SCAPS-1D, a 1D solar cell simulation tool developed by Mark Burgelman and his team at the University of Gent, is used in this study. The software can replicate experimental efficiency values accurately with high precision by setting defect parameters properly. Simulating major photovoltaic processes, including light absorption, exciton formation, charge transport and collection, and recombination. Equation describes how the electrostatic potential depends on the distribution of charge density in the program which is used in the program's calculations. The simulation framework is built upon three fundamental semiconductor equations: Equation (1): the continuity equation for holes, Equation (2): the continuity equation for electrons, Equation (3): the Poisson equation [34–35]

$$\frac{dP_n}{dt} = G_p - \frac{P_n - P_{n0}}{\tau_p} - P_n u_p \frac{dE}{dx} - u_p E \frac{dP_n}{dx} + D_p \frac{d^2P_n}{dx^2} \quad (1)$$

$$\frac{dn_P}{dt} = G_n - \frac{n_P - N_{p0}}{\tau_n} - n_p u_n \frac{dE}{dx} - u_n E \frac{dP_p}{dx} + D_p \frac{d^2n_P}{dx^2} \quad (2)$$

$$\frac{d}{dx}\left(\varepsilon(x)\frac{d\varphi}{dx}\right) = q\left[p(x) - n(x) + N_{d^+}(x) - N_{a^-}(x) + P_t(x) - n_t(x)\right] \quad (3)$$

where, q is the electron charge, and ε is the permittivity of free space. The rate of generation is denoted as G and D as a diffusion coefficient. φ is the electrostatic potential, and E is an electric field. The free electron density, $n(x)$, and the free hole density $p(x)$, respectively, are given. In addition, $p(x)$ represents the density of trapped holes and $n(x)$ represents the density of trapped electrons. N_{d^+} refers to the concentration of donor-ionized doping, and N_{a^-} reports acceptor-ionized doping concentration. x is the spatial coordinate, finally, referring to the thickness.

3 | Results and Discussion

3.1 | DFT Analysis of Structural and Optoelectronic Properties

Figure 1a illustrates the cubic crystal structure of Cs_2AuScI_6, a double perovskite (DP) halide with a simple 2:1:1:6 composition ratio. The unit cell consists of 8 cesium (Cs) atoms, 13 gold-centered [Au-I_6] octahedra, and 14 scandium-centered [Sc-I_6] octahedra, arranged in a face-centered cubic (Fm-3m) symmetry. The atomic positions are as follows: Cs at (0.25, 0.25, 0.25), Au at (0.5, 0.5, 0.5), Sc at (0, 0, 0), and iodine (I) at (0.25, 0, 0).

Using the GGA–PBE method, the lattice parameter was first optimized to 11.8920 Å at a volume of 2835 $Bohr^3$. The structural stability was assessed based on several factors, including the tolerance factor, octahedral factor, formation energy, binding energy, and phonon dispersion. These factors, along with DFT-computed parameters, were discussed in a published article by Mahmud et al. [36]. The essential (AIMD simulation for thermodynamic stability) and remaining DFT-based optoelectronic parameters are discussed in this work. The phonon dispersion phenomena in Figure 1b verifying the dynamic stability of this compound have been reported in our previous study [36]. To confirm the thermodynamic stability of the Cs_2AuScI_6 double perovskite, ab initio molecular dynamics (AIMD) simulations were conducted at 300 K for 10 fs (femto-second) under the NVT ensemble. As shown in Figure 1c, the total energy of the system fluctuates slightly around a constant mean value, and the temperature remains stable without any abrupt deviation, indicating strong physical integrity throughout the simulation.

Extensive studies on the optoelectronic properties of Cs_2AuScI_6 have primarily focused on its band structure, revealing its semiconducting nature. The vacant Fermi level indicates an indirect bandgap between the conduction band minimum (CBM) and the valence band maximum (VBM). Two computational methods were used to calculate the bandgap: GGA–PBE and TB-mBJ. The bandgap was approximated by the GGA-PBE functional to be 0.95 eV, while the more accurate TB-mBJ method estimated it to be 1.30 eV(Figure 2). Specifically, the TB-mBJ method defines a bandgap transition from the L symmetry point to the X symmetry point, whereas the GGA–PBE method indicates a transition from L to Γ symmetry points. The advantage of this indirect bandgap is its contribution to long carrier lifetimes and low recombination losses, which facilitate the development of Cs_2AuScI_6-based thin-film solar cells. In solar cells, the charge carrier performance of electrons and holes is critical to determining efficiency [37]. The critical parameters—effective mass, density of states, and mobility—govern carrier transport, recombination, and overall device efficiency.

The effective mass (m∗) is derived from the band structure and represents the curvature of the conduction and valence bands [38]. The calculated effective masses of holes and electrons were 0.25 and 0.14, respectively, which is a very beneficial and driving parameter for solar absorber materials. The effective density of

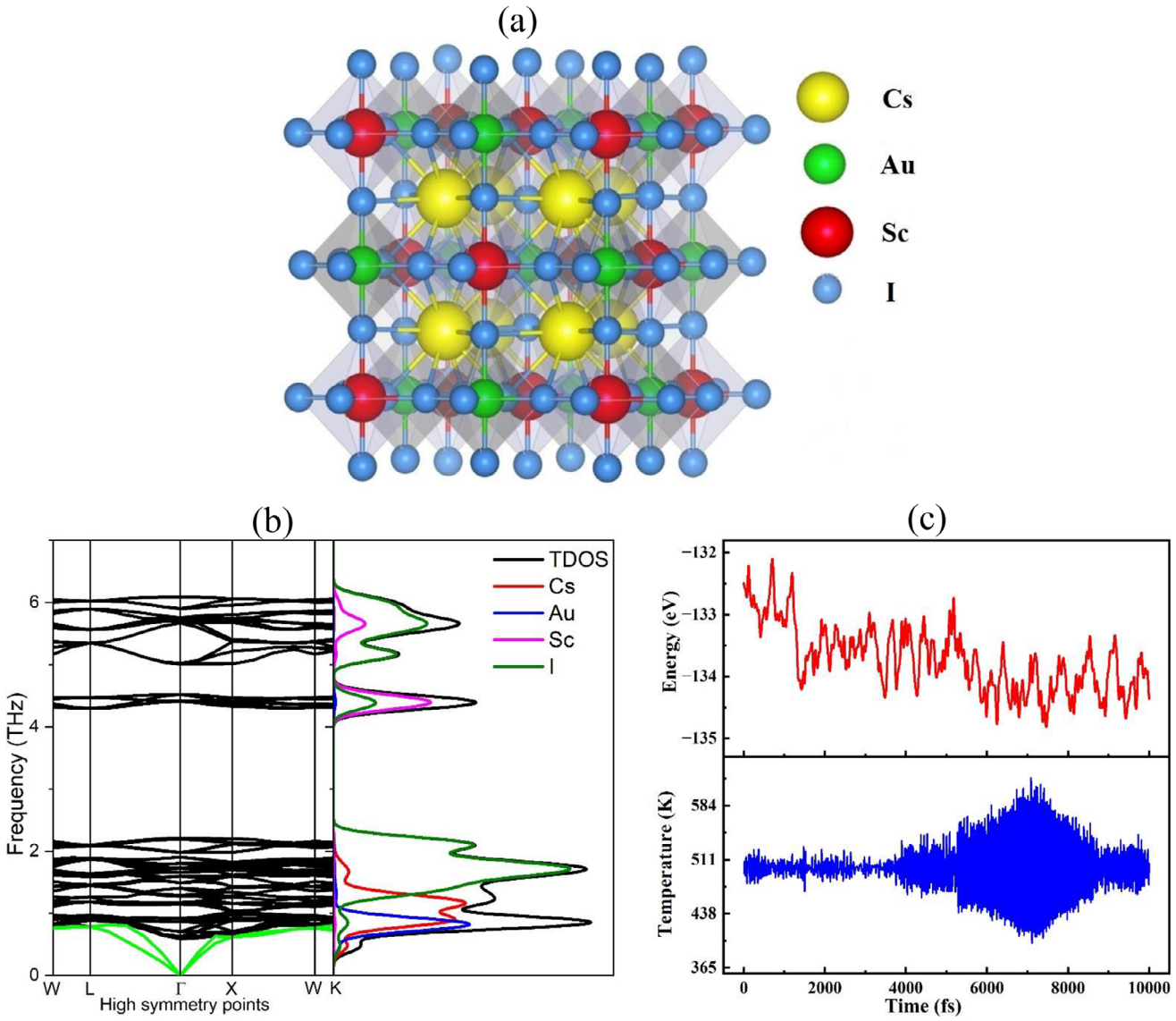

FIGURE 1 | (a) Unit cell. (b) Phonon dispersion curve. (c) AIMD simulation result of Cs_2AuScI_6 double halide perovskite.

states represents the number of available electronic states in the conduction (N_c) and valence (N_v) bands and is calculated by the following formula [39–40]

$$N_c = 2.5409 \times 10^{19} \left(\frac{m_e^*}{m_0} \right)^{3/2} \tag{4}$$

$$N_v = 2.5409 \times 10^{19} \left(\frac{m_h^*}{m_0} \right)^{3/2} \tag{5}$$

The carrier mobility (μ) of electrons and holes may be calculated by considering the relaxation time with a value of ($\tau = 10^{-14}$ s) and effective mass using the following equations [41]

$$\mu_e = \frac{q\tau}{m_e^*} \text{ and } \mu_h = \frac{q\tau}{m_h^*} \tag{6}$$

where, q is the basic charge of 1.6×10^{-19} C. Materials with a low effective mass, high state density, and high carrier mobility exhibit better charge transport, leading to higher power conversion efficiency. The calculated values are shown in Table 2.

Optical absorption and reflectance are critical parameters that significantly impact solar cell performance, as they determine the material's ability to absorb and convert light energy into electrical energy [42]. Cs_2AuScI_6 possesses unusually high peaks in its optical absorption spectrum within the visible region (1.77–3.10 eV, i.e., 700–400 nm), indicating its highly light-absorbing nature (Figures 3a, 3b). The material demonstrates an absorption coefficient on the order of 10^6 cm^{-1}, which is comparable to widely used solar cell materials like Si (10^3–10^5 cm^{-1}), InP (≈10^5 cm^{-1}), and CdTe (10^4–10^5 cm^{-1}) [43], making it a promising contestant for photovoltaic applications. In addition to having a better absorption quality, Cs_2AuScI_6 also has a low static reflectivity of 14.58%, such that most of the incident light is absorbed and not reflected out. The maximum reflectivity in the visible range was 25%, which is an excellent value for efficient light harvesting (Figure 3c). This property is especially significant for solar cells, since low reflection allows for enhanced photon absorption and greater

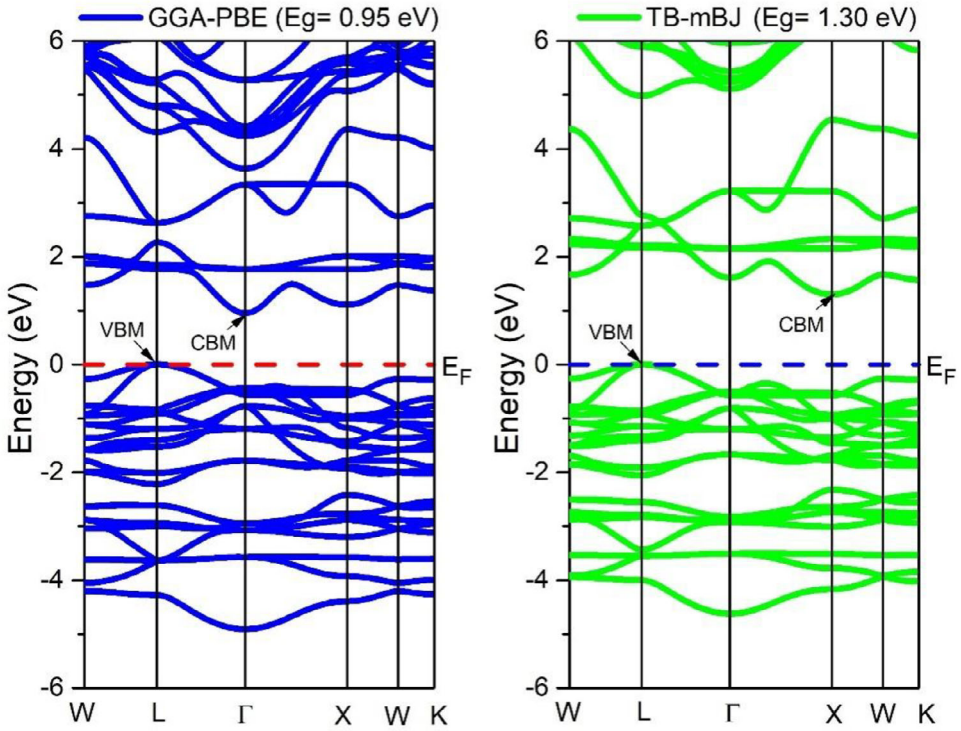

FIGURE 2 | Band structure of Cs_2AuScI_6 by using GGA–PBE and TB–mBJ.

charge carrier generation, thus enhancing energy conversion efficiency. The combination of high absorption, low reflectivity, and an advantageous band structure positions Cs_2AuScI_6 as a highly suitable material for next-generation high-efficiency solar energy conversion. Furthermore, its unique optoelectronic properties suggest potential applications including other renewable energy technologies and advanced optoelectronic devices.

3.2 | SCAPS-1D Results Analysis

3.2.1 | Optimization of HTL Layer and ETL Layer

The layered structure of Cs_2AuScI_6 solar cell devices is illustrated in Figure 4. The HTL plays a crucial role in the performance of perovskite solar cells by enabling the efficient transport of positive charge carriers (holes) from the photoactive layer to the anode. HTL enables efficient hole extraction and prevents recombination loss, resulting in better overall device efficiency. Similarly, the ETL is responsible for the collection and transport of electrons generated in the perovskite absorber layer to the cathode. By efficient breaking of photo-generated electron–hole pairs, the ETL avoids hole leakage into the cathode, thus preventing recombination loss. It also acts as a shielding role against external stimuli (oxygen and humidity), thereby improving the long-term stability of the solar cell. Common ETL materials are organic compounds like PCBM (Phenyl-C61-butyric acid methyl ester), metal oxides (ZnO), and other materials like WS_2, TiO_2, IGZO, and C_{60}, chosen due to their suitable energy levels, high electron mobility, and stability. In this research, we utilized these ETL materials and examined various HTL and ETL combinations to achieve optimal device performance. Six (6) HTL and six (6) ETL materials were tested, resulting in thirty-six (36) different device configurations. The input parameters for the HTL, ETL, and absorber material are provided in Tables 1 and 2, while the optimization manner is depicted in Figure 5.

In Figure 5a, six different HTLs—CBTS, CdTe, P3HT, PEDOT:PSS, PTAA, and CuI—were optimized using the first ETL, WS_2. The corresponding Es for these configurations were 25.55%, 24.48%, 18.40%, 15.96%, 20.29%, and 22.76%, respectively. For the second ETL, ZnO, the highest PCE of 25.56% was achieved using CBTS as the HTL. The other HTL combinations resulted in PCE values of 24.49% (CdTe), 18.40% (P3HT), 15.97% (PEDOT:PSS), 20.28% (PTAA), and 22.76% (CuI), as shown in Figure 5b. In Figure 5c, the ETL TiO_2 was optimized with the six HTLs, yielding PCE values of 25.55% (CBTS), 24.48% (CdTe), 18.39% (P3HT), 15.96% (PEDOT:PSS), 20.28% (PTAA), and 22.75% (CuI). The fourth ETL, PCBM, resulted in PCE values of 25.43%, 24.36%, 18.28%, 15.85%, 20.16%, and 22.63% for CBTS, CdTe, P3HT, PEDOT:PSS, PTAA, and CuI, respectively, as shown in Figure 5d. Similarly, the fifth ETL, IGZO, achieved its highest PCE of 25.55% with CBTS, while other HTL combinations yielded 24.48% (CdTe), 18.40% (P3HT), 15.96% (PEDOT:PSS), 20.29% (PTAA), and 22.75% (CuI), as shown in Figure 5e. For the sixth ETL, C_{60}, the highest PCE was 17.64% with CBTS. Other HTL configurations produced PCE values of 17.00% (CdTe), 11.71% (P3HT), 9.82% (PEDOT:PSS), 13.22% (PTAA), and 15.33% (CuI), as shown in Figure 5f. After evaluating all possible HTL and ETL combinations with the Cs_2AuScI_6 absorber and Ni metal contact, it was found that CBTS consistently demonstrated the highest performance across all ETL layers. However, the second-highest performance for each ETL was observed when CdTe was used as the HTL.

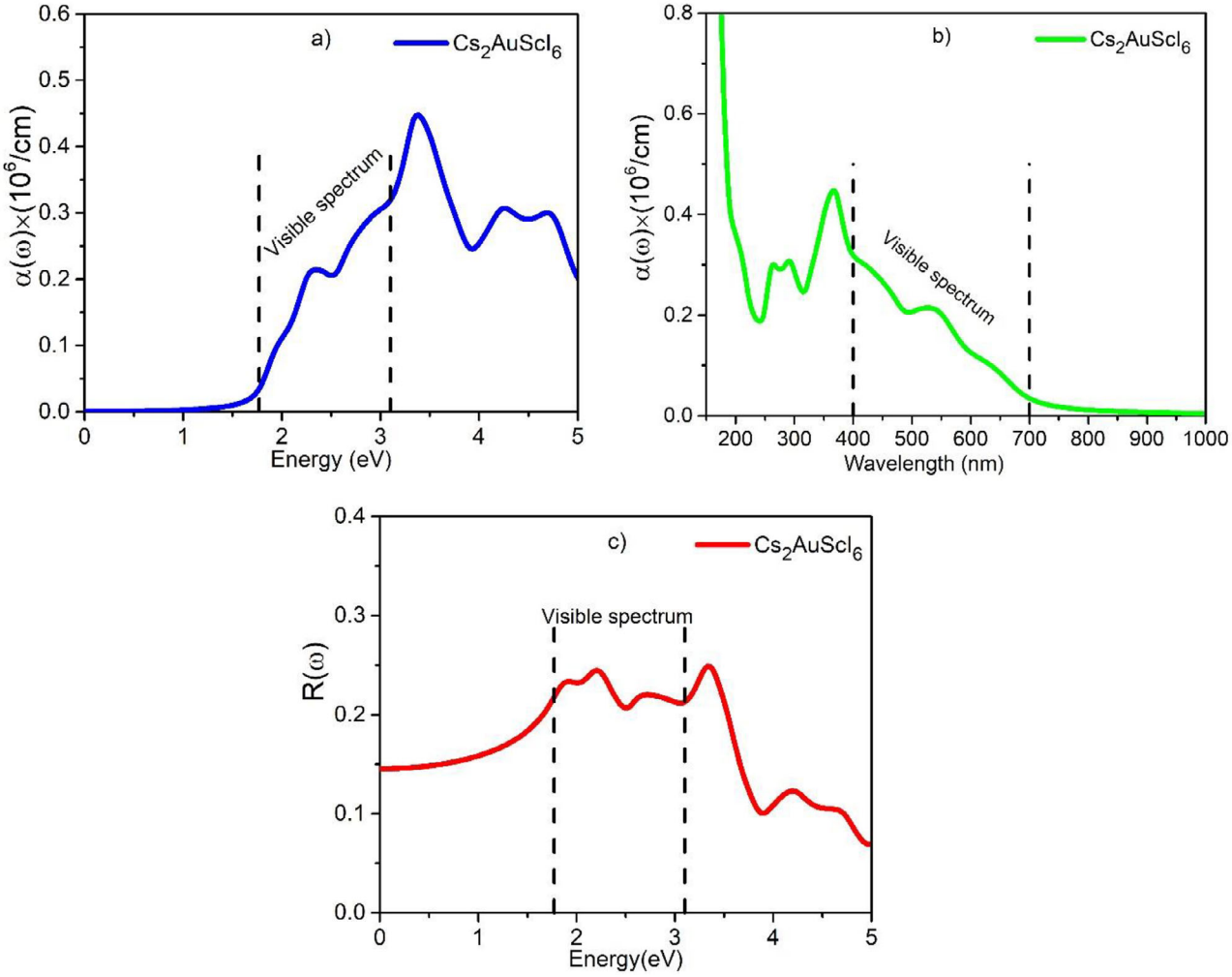

FIGURE 3 | (a and b) Absorption coefficient as a function of photon energy (eV) and wavelength (nm), and (c) Reflectivity of Cs_2AuScI_6 compound.

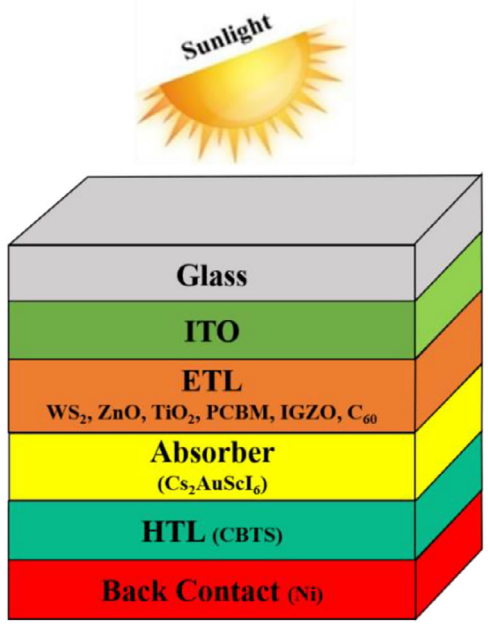

FIGURE 4 | Layered structure of Cs_2AuScI_6-based solar cell.

3.2.2 | Band Diagram

The band diagram visually represents the conduction band (CB) and valence band (VB) of the double perovskite (DP) material, ETL, and HTL. Figure 6 illustrates electron transfer from the perovskite absorber to the ETL and hole transfer to the HTL, highlighting the energy level alignment among different materials—an essential factor for optimizing charge transport efficiency. Proper energy orientation certifies effective charge carrier separation and transport while reducing recombination losses at the perovskite/transport layer interfaces. The energy level difference between the ETL's conduction band and the HTL's valence band determines the open-circuit voltage. For efficient charge extraction, the electron affinity of the ETL and the ionization energy of the HTL must be appropriately positioned relative to the absorber. The determination of Fermi levels across different layers is critical for understanding the thermodynamic stability and electronic characteristics of the device. When WS_2 is used as the ETL and CBTS as the HTL, the Fermi level aligns with the conduction band (CB). Under illumination, the band diagram helps visualize the separation of quasi-Fermi levels for electrons (F_n) and holes (F_p), which directly influences the photovoltage of the solar cell. In each degenerate semiconductor device, F_n and F_p lie near the conduction band energy (E_c) and valence band energy

TABLE 1 | Input parameters of front contact (ITO) and different HTLs [44, 21].

Parameters	ITO	CBTS	CdTe	P3HT	PEDOT:PSS	PTAA	CuI
t (nm)	500	100	200	50	50	150	100
E_g (eV)	3.5	1.9	1.5	1.7	1.6	2.96	3.1
χ (eV)	4	3.6	3.9	3.5	3.4	2.3	2.1
E_r	9	5.4	9.4	3	3	9	6.5
N_C (1/cm^3)	2.2×10^{18}	2.2×10^{18}	8×10^{17}	2.0×10^{21}	2.2×10^{18}	2.0×10^{21}	2.8×10^{19}
N_V (1/cm^3)	1.8×10^{19}	1.8×10^{19}	1.8×10^{19}	2.0×10^{21}	1.8×10^{19}	2.0×10^{21}	1×10^{19}
μ_n (cm^2/Vs)	20	30	3.2×10^{2}	1.8×10^{-3}	4.5×10^{-2}	1	100
μ_h (cm^2/Vs)	10	10	4×10^{1}	1.86×10^{-2}	4.5×10^{-2}	40	43.9
N_D (1/cm^3)	1×10^{21}	0	0	0	0	0	0
N_A (1/cm^3)	0	1×10^{18}	2.0×10^{14}	1×10^{18}	1×10^{18}	1×10^{18}	1×10^{18}
N_t (1/cm^3)	1×10^{15}	1×10^{15}	1×10^{15}	1×10^{15}	1×10^{15}	1×10^{15}	1×10^{15}

TABLE 2 | Input parameters of Different ETLs and absorber material [44, 21].

Parameters	WS_2	ZnO	TiO_2	PCBM	IGZO	C_{60}	Cs_2AuScI_6
t (nm)	100	50	30	50	30	50	800
E_g (eV)	1.8	3.3	3.2	2	3.05	1.7	1.30
χ (eV)	3.95	4	4	3.9	4.16	3.9	4.30
E_r	13.6	9.00	9	3.9	10	4.2	7.72
N_C (1/cm^3)	1×10^{18}	3.7×10^{18}	2×10^{18}	2.5×10^{21}	5×10^{18}	8×10^{19}	1.33×10^{18}
N_V (1/cm^3)	2.4×10^{19}	1.8×10^{19}	1.8×10^{19}	2.5×10^{21}	5×10^{18}	8×10^{19}	3.17×10^{18}
μ_n (cm^2/Vs)	100	100	20	0.2	15	8×10^{-2}	83.20
μ_h (cm^2/Vs)	100	250	10	0.2	0.1	3.5×10^{-3}	46.59
N_D (1/cm^3)	1×10^{18}	1×10^{18}	9×10^{16}	2.93×10^{17}	1×10^{17}	1×10^{17}	0
N_A (1/cm^3)	0	0	0	0	0	0	1×10^{15}
N_t (1/cm^3)	1×10^{15}	1×10^{15}	1×10^{15}	1×10^{15}	1×10^{15}	1×10^{15}	1×10^{15}

Note: Where, t = thickness, E_g = bandgap, χ = Electron affinity, E_r = relative dielectric constant; N_c, N_v = state densities of conduction and valence band; μ_n, μ_h = Electron and hole mobility; N_D, N_A, N_t = density of donor, acceptor and defect, respectively.

(E_v), respectively, as depicted in Figure 6a–f. This study offers a comprehensive understanding of the electrical properties, charge carrier dynamics, and potential efficiency of the device.

3.2.3 | Effect of Absorber Thickness and ETL Thickness

The enactment of double perovskite solar cells (DPSCs) is highly reliant on the thickness of both the absorber layer and the ETL. An excessively thin absorber layer may not capture sufficient light, leading to reduced photocurrent and power conversion efficiency. Conversely, an overly thick absorber layer can increase recombination losses as charge carriers must travel longer distances to touch the electrodes. This also raises the series resistance, further decreasing efficiency. In thin films, shorter carrier transport distances enhance charge collection and minimize recombination losses. However, thicker perovskite layers may degrade faster, especially if they contain defects and grain boundaries that facilitate moisture and oxygen infiltration. The ETL thickness is equally critical for efficient charge extraction and transport. If too thin, it may not adequately cover the substrate, resulting in poor electron extraction and enhanced recombination at the interface. Conversely, an overly thick ETL can increase series resistance, reducing overall device efficiency. Therefore, to optimize DP solar cells for maximum efficiency, the absorber layer thickness must be adjusted to maximize light absorption, minimize recombination losses, and ensure efficient charge carrier extraction. Similarly, the ETL thickness should be optimized to facilitate effective electron transport and extraction while minimizing resistance and optical losses.

Figure 7 illustrates the impact of absorber layer thickness and electron transport layer (ETL) thickness on the open-circuit voltage (V_{OC}) is analyzed for the six most efficient solar cell configurations. The ETL thickness varies between 0.03 and 0.11 μm, while the absorber layer thickness ranges from 0.4 to 1.4 μm across all structures. Notably, variations in ETL thickness do not significantly affect the absorber layer thickness in configurations

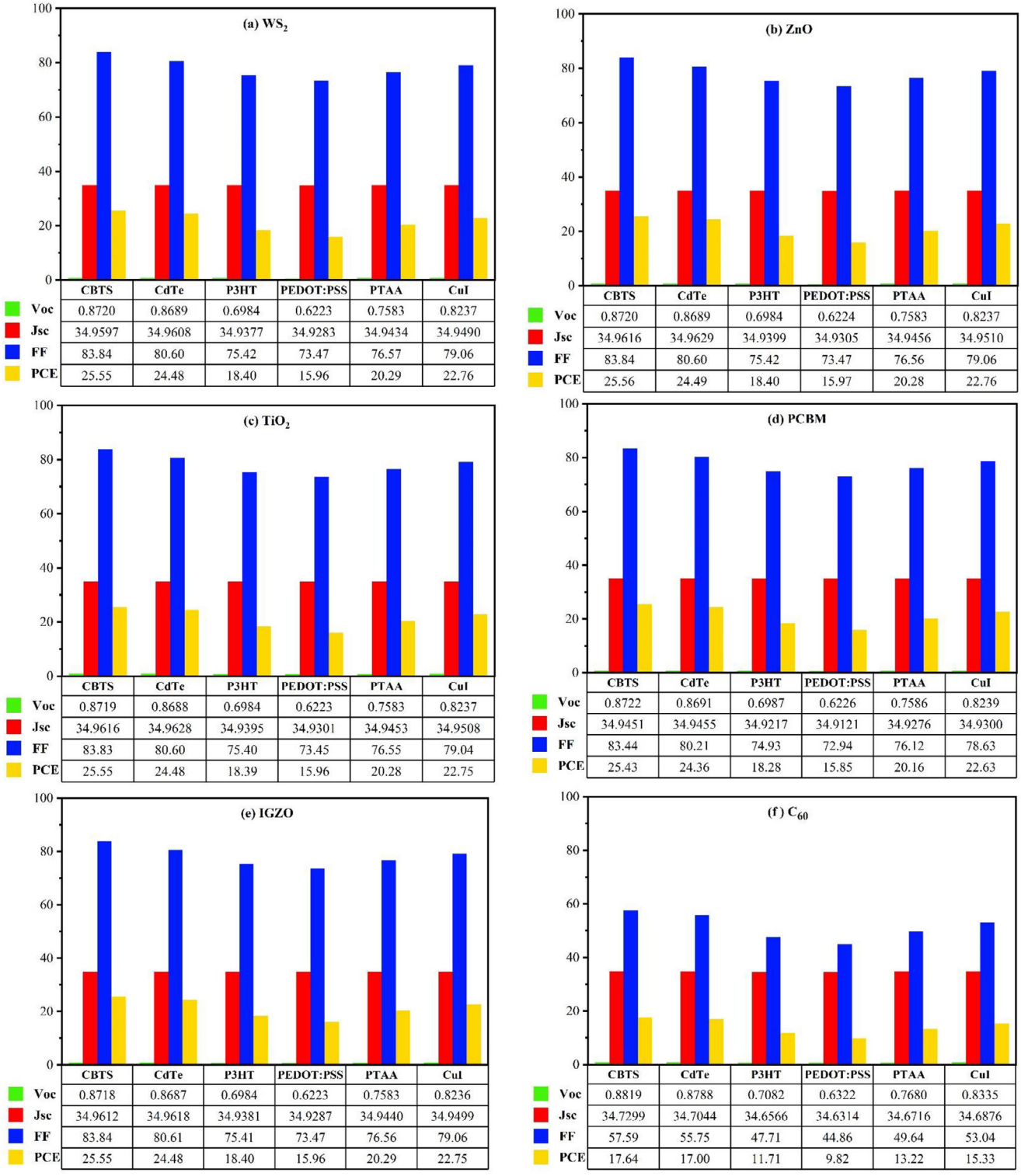

	CBTS	CdTe	P3HT	PEDOT:PSS	PTAA	CuI
Voc	0.8720	0.8689	0.6984	0.6223	0.7583	0.8237
Jsc	34.9597	34.9608	34.9377	34.9283	34.9434	34.9490
FF	83.84	80.60	75.42	73.47	76.57	79.06
PCE	25.55	24.48	18.40	15.96	20.29	22.76

	CBTS	CdTe	P3HT	PEDOT:PSS	PTAA	CuI
Voc	0.8720	0.8689	0.6984	0.6224	0.7583	0.8237
Jsc	34.9616	34.9629	34.9399	34.9305	34.9456	34.9510
FF	83.84	80.60	75.42	73.47	76.56	79.06
PCE	25.56	24.49	18.40	15.97	20.28	22.76

	CBTS	CdTe	P3HT	PEDOT:PSS	PTAA	CuI
Voc	0.8719	0.8688	0.6984	0.6223	0.7583	0.8237
Jsc	34.9616	34.9628	34.9395	34.9301	34.9453	34.9508
FF	83.83	80.60	75.40	73.45	76.55	79.04
PCE	25.55	24.48	18.39	15.96	20.28	22.75

	CBTS	CdTe	P3HT	PEDOT:PSS	PTAA	CuI
Voc	0.8722	0.8691	0.6987	0.6226	0.7586	0.8239
Jsc	34.9451	34.9455	34.9217	34.9121	34.9276	34.9300
FF	83.44	80.21	74.93	72.94	76.12	78.63
PCE	25.43	24.36	18.28	15.85	20.16	22.63

	CBTS	CdTe	P3HT	PEDOT:PSS	PTAA	CuI
Voc	0.8718	0.8687	0.6984	0.6223	0.7583	0.8236
Jsc	34.9612	34.9618	34.9381	34.9287	34.9440	34.9499
FF	83.84	80.61	75.41	73.47	76.56	79.06
PCE	25.55	24.48	18.40	15.96	20.29	22.75

	CBTS	CdTe	P3HT	PEDOT:PSS	PTAA	CuI
Voc	0.8819	0.8788	0.7082	0.6322	0.7680	0.8335
Jsc	34.7299	34.7044	34.6566	34.6314	34.6716	34.6876
FF	57.59	55.75	47.71	44.86	49.64	53.04
PCE	17.64	17.00	11.71	9.82	13.22	15.33

FIGURE 5 | Initial optimization process of HTL and ETL layer.

using WS_2, ZnO, TiO_2, PCBM, IGZO, and C_{60} as ETLs. The highest V_{OC} values are observed when the absorber thickness falls within the range of 0.4–0.52 μm. In contrast, increasing absorber layer thickness generally leads to a reduction in V_{OC} for most configurations.

This decline is attributed to a rise in saturation current, which exceeds the photocurrent due to increased carrier recombination in thicker absorber layers. Optimized device performance is achieved by carefully balancing absorber and ETL thicknesses to minimize recombination losses while maintaining efficient charge transport.

Figure 8 illustrates the influence of absorber layer and ETL thickness on the short-circuit current density (J_{SC}) is analyzed across six different perovskite solar cell models. The results show

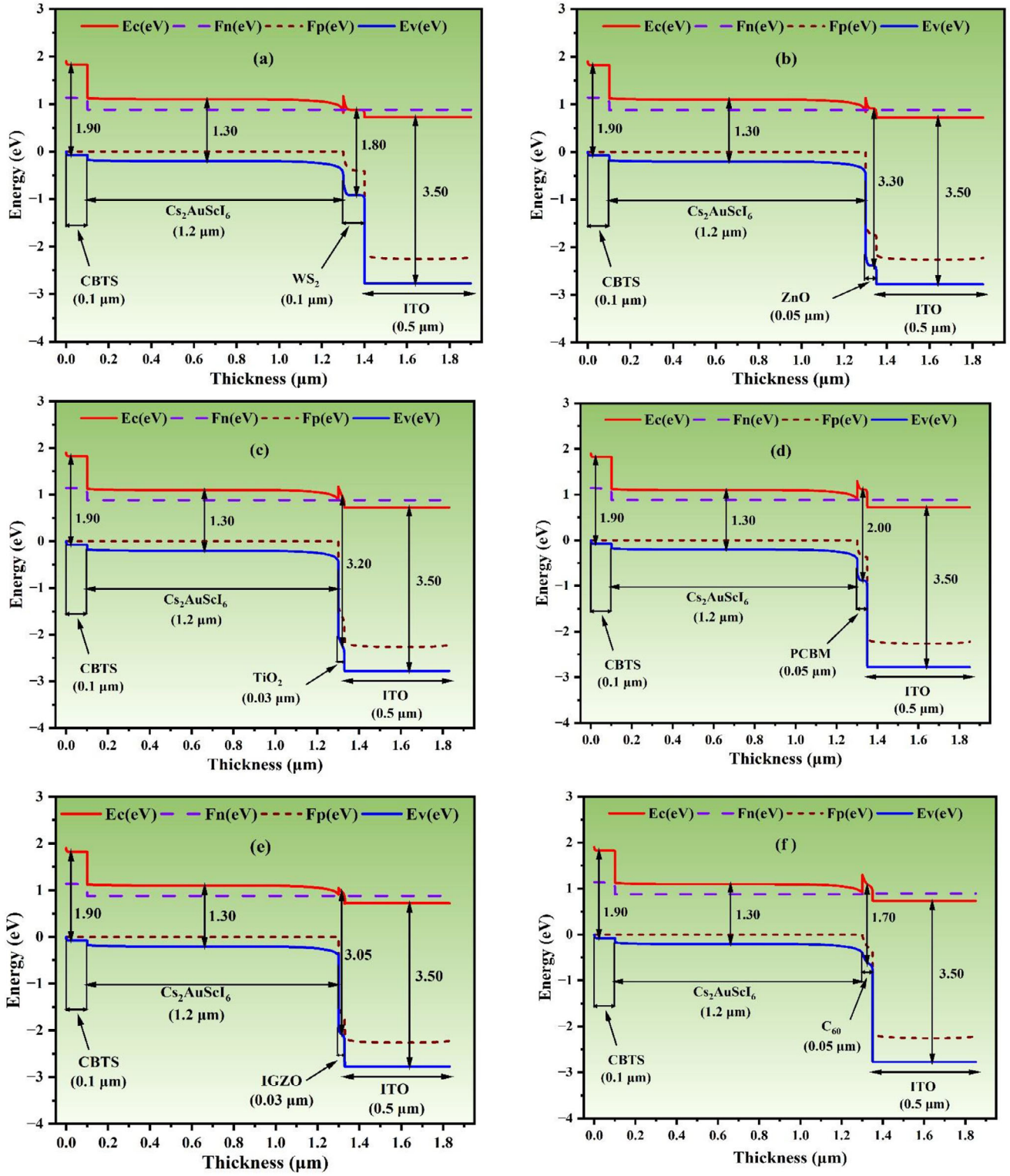

FIGURE 6 | Energy band diagram of double perovskite (Cs_2AuScI_6) solar cell device with ETL's of (a) WS_2, (b) ZnO, (c) TiO_2, (d) PCBM, (e) IGZO, and (f) C_{60} with HTL of CBTS.

that J_{SC} increases with absorber layer thickness, while it remains largely unaffected by ETL thickness. For five configurations (WS_2, ZnO, TiO_2, PCBM, and IGZO as ETLs), the highest J_{SC} values occur when the absorber thickness exceeds 0.7 μm, with a maximum J_{SC} of 35.12 mA cm^{-2}. Notably, when the absorber thickness exceeds 0.6 μm and the ETL thickness ranges from 0.03 to 0.08 μm, C_{60} as the ETL achieves optimal J_{SC} performance. Variations in J_{SC} among optimized devices arise from differences in electronic properties, charge transport dynamics, recombination rates, and morphological characteristics. Each ETL material uniquely influences electron transport and recombination, with ETL thickness playing a critical role in balancing charge extrac-

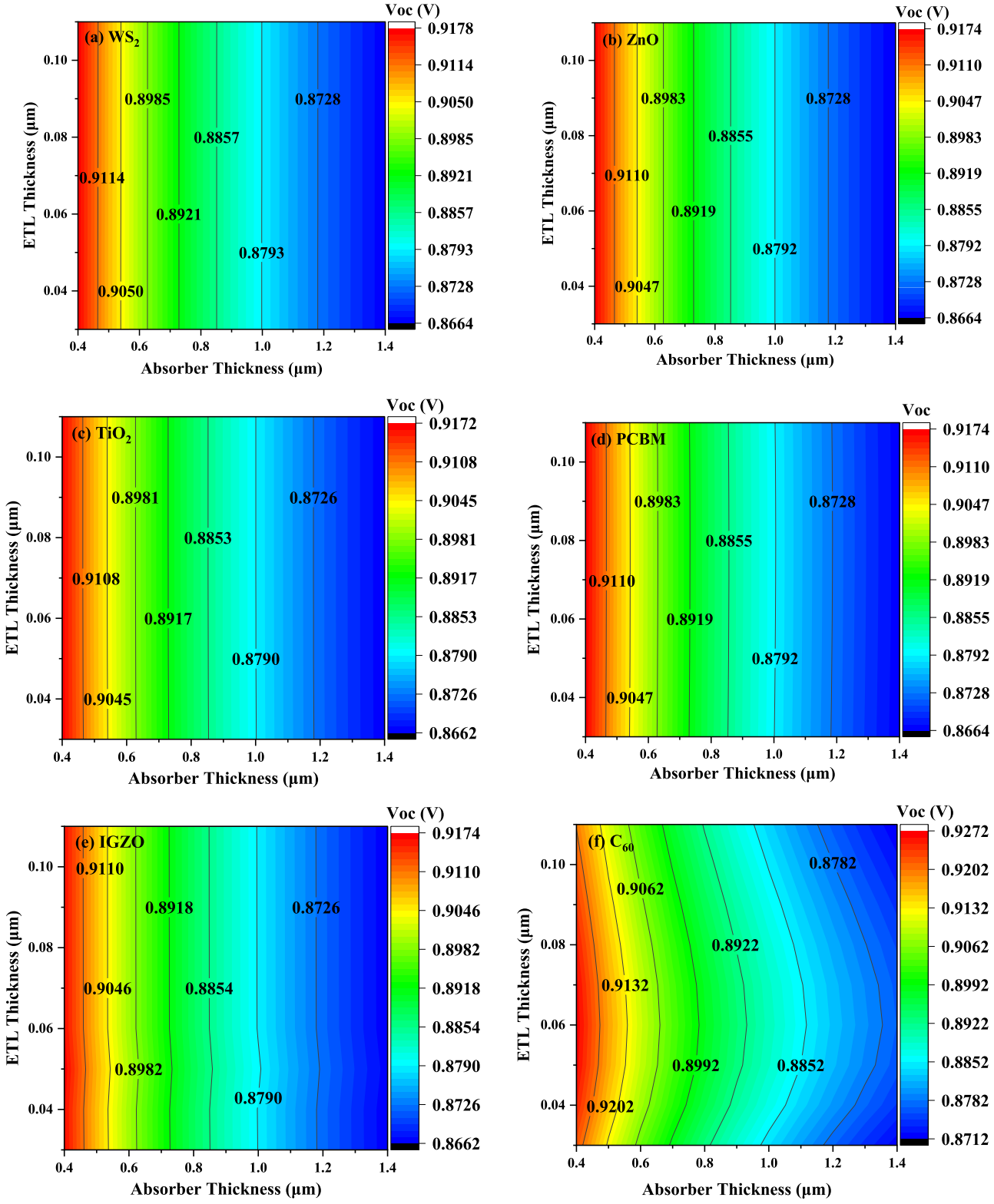

FIGURE 7 | Contour mapping of V_{oc} (V) When ETLs as (a) WS_2, (b) ZnO, (c) TiO_2 (d) PCBM, (e) IGZO, and (f) C_{60}.

tion and minimizing recombination losses. The interplay of these factors—including ETL thickness, series resistance, and defect formation—accounts for the observed differences in J_{SC} performance across different material configurations

Figure 9 clarifies the influence of absorber and ETL thickness on the fill factor (FF) across different perovskite solar cell configurations. For devices using WS_2, ZnO, TiO_2, PCBM, and IGZO as ETLs, the FF increases with absorber layer thickness while remaining largely unaffected by the ETL thickness. The highest FF is witnessed once the absorber thickness exceeds 1.2 μm in these configurations. However, in the C_{60}-based solar cell, an anomaly is noted—FF decreases as both absorber and ETL thicknesses increase. The highest FF of 70.95% is achieved while

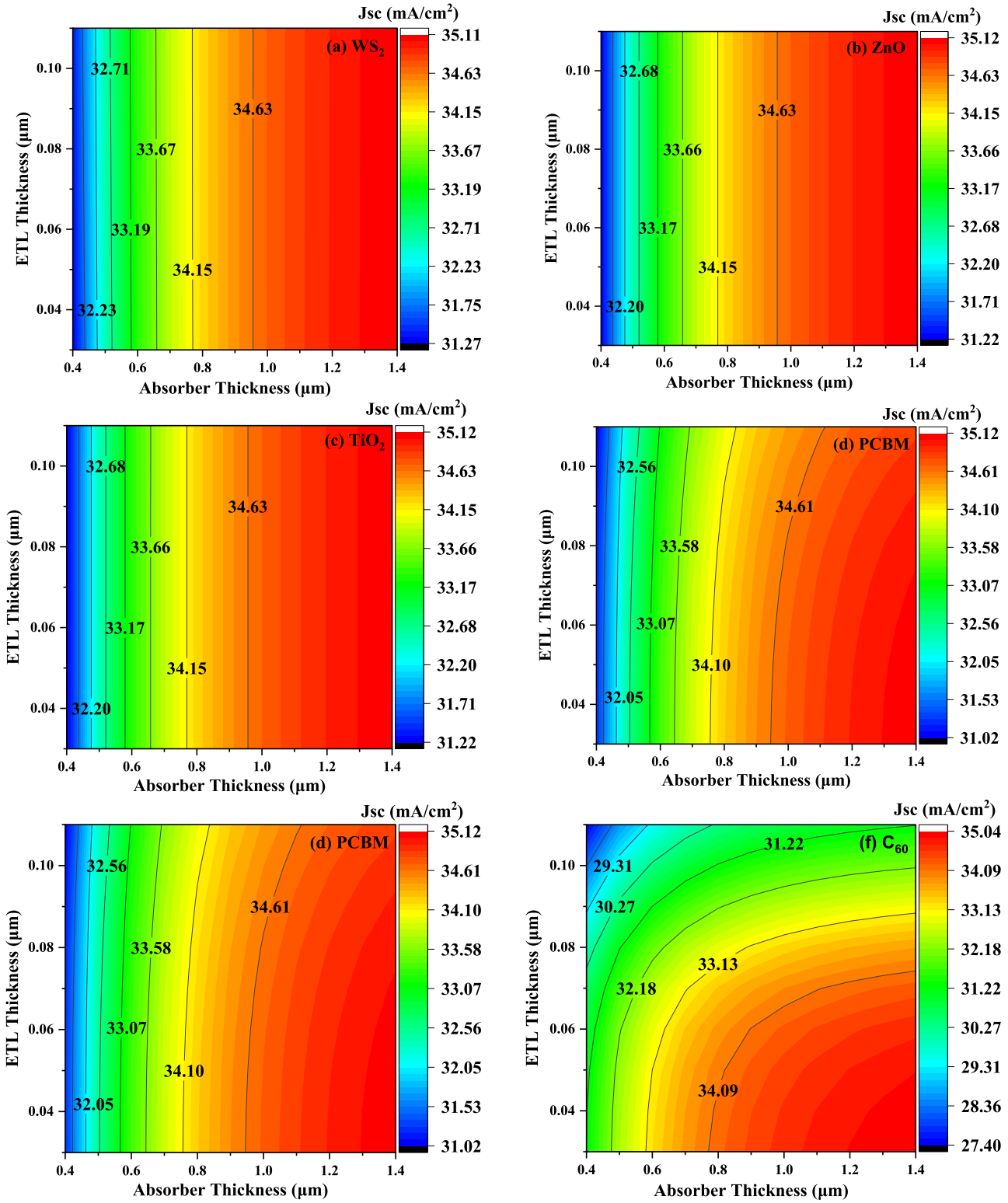

FIGURE 8 | Contour mapping of J_{sc} (mA/cm^2) When ETLs as (a) WS_2, (b) ZnO, (c) TiO_2 (d) PCBM, (e) IGZO, and (f) C_{60}.

the ETL thickness remains below 0.45 µm, independent of the absorber thickness.

Figure 10 explains the effect of absorber layer thickness on PCE. For all studied ETLs except C_{60}, PCE increases with absorber thickness, while variations in ETL thickness have no significant impact. The highest efficiencies of 25.58%, 25.58%, 25.57%, 25.45%, and 25.58% are achieved when the absorber thickness go beyond 1.2 µm, as shown in Figure 10a–e. In contrast, the C_{60}-based solar structure exhibits a different trend, with PCE decreasing as ETL thickness increases. The highest PCE of 21.20% is witnessed when the ETL thickness remains below 0.04 µm, independent of absorber thickness, as depicted in Figure 10f. Optimizing both ETL and absorber layer thickness is crucial for maximiz-

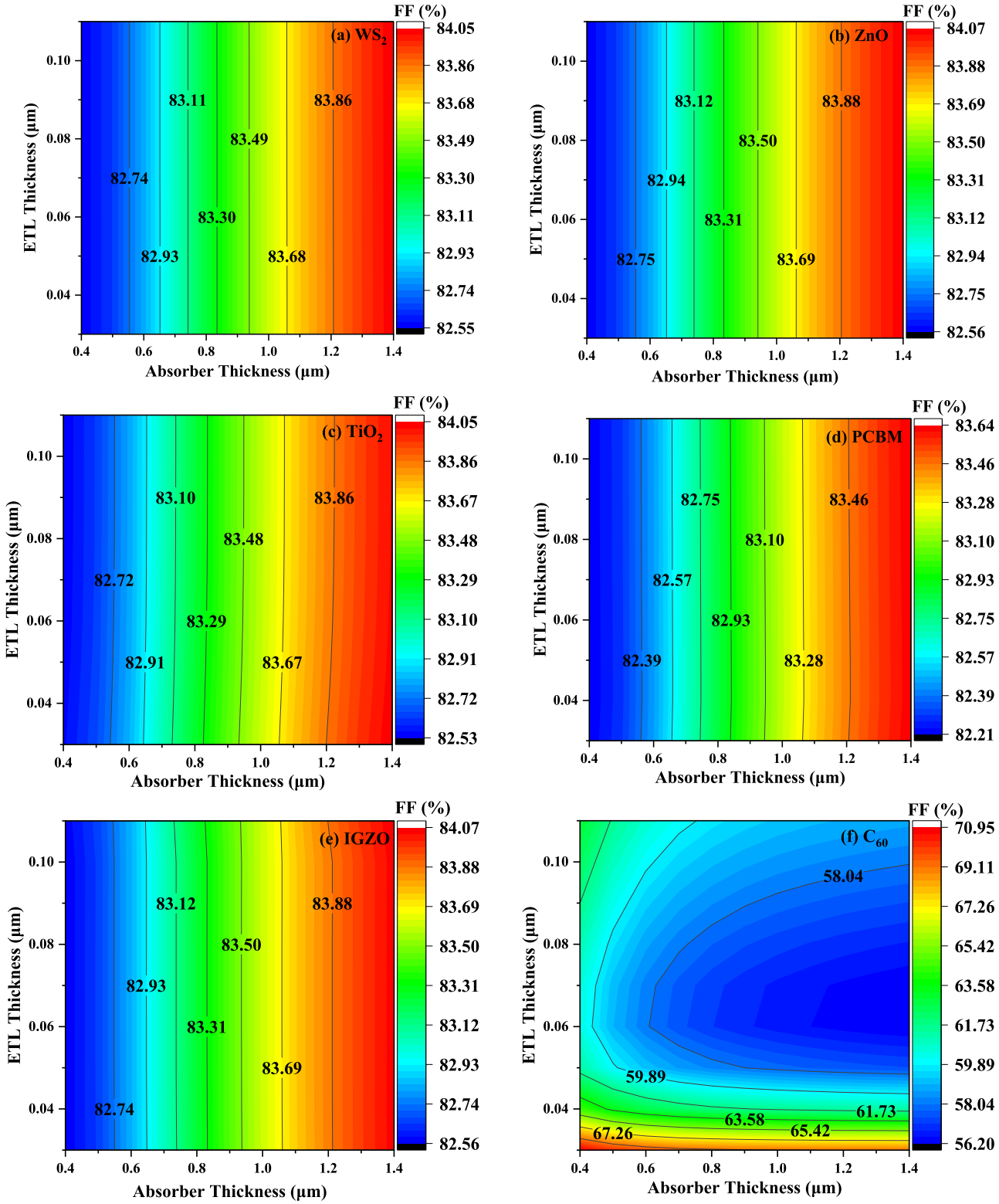

FIGURE 9 | Contour mapping of FF (%) when ETLs as (a) WS_2, (b) ZnO, (c) TiO_2 (d) PCBM, (e) IGZO, and (f) C_{60}.

ing efficiency in double perovskite solar cells. A well-balanced combination enhances light absorption, minimizes electron–hole recombination, and reduces series resistance. These findings afford valuable insights for material selection and structural optimization, contributing to the development of more efficient and commercially viable solar technologies.

The variations in V_{OC}, J_{SC}, FF, and PCE of perovskite solar cells with different ETLs are influenced by multiple connected factors. One key determining factor is the absorption coefficient, which is directly associated to the bandgap of the ETL. This coefficient significantly impacts photovoltaic parameters by governing how effectively incident photons interact with the

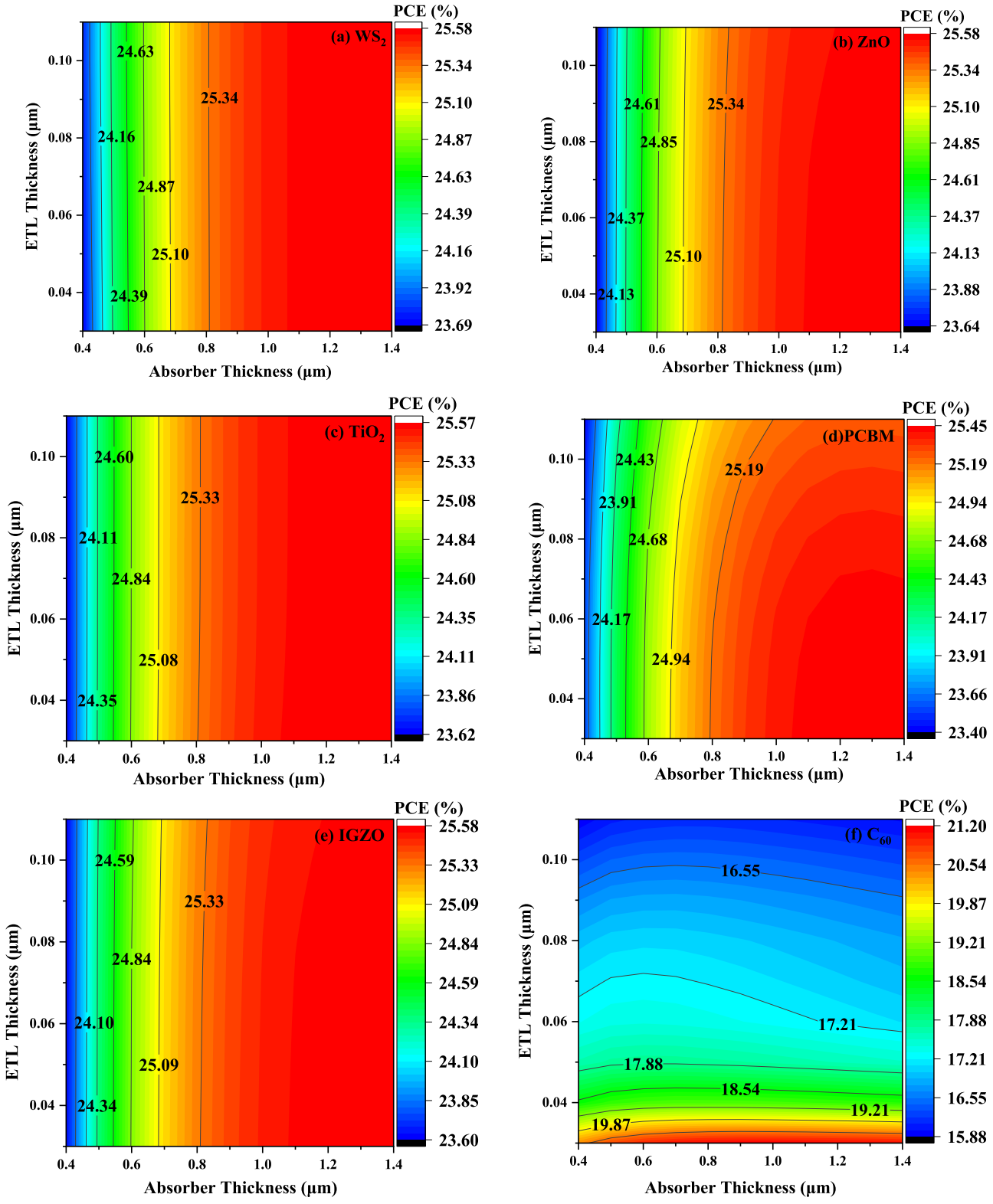

FIGURE 10 | Contour mapping of PCE(%) when ETLs as (a) WS_2, (b) ZnO, (c) TiO_2 (d) PCBM, (e) IGZO and (f) C_{60}.

Cs_2ScAuI_6 absorber layer beneath. Another critical factor is the work function difference between the ETL and the absorber layer, which is derived from their electron affinity and Fermi energy levels. This difference influences the conduction band offset (CBO), a crucial parameter affecting charge transport and overall solar cell efficiency. The impact of electron affinity mismatch at the ETL/absorber interface plays a defining role in energy band alignment. A negative CBO (−) occurs when the ETL's conduction band (CB) is positioned lower than that of the absorber, resulting in an energy cliff. In this scenario, the cliff does not present a significant barrier to electron transport. Conversely, a positive CBO (+) forms when the ETL's CB is higher

than that of the absorber, creating an energy spike that obstructs electron flow at the interface, thereby reducing efficiency [45]. Interestingly, this spike structure at the ETL/absorber interface can enhance photo generation of free charge carriers. The energy barrier it creates helps prevent the backflow of photogenerated electrons, thereby reducing recombination rates and improving photovoltaic performance. However, when a cliff-type band alignment is present, recombination is more likely to occur at the interface if the activation energy for carrier recombination (E_A) is lower than the absorber layer's bandgap. This reduction in E_A ultimately lowers the open-circuit voltage (V_{OC}) and impacts other key photovoltaic parameters, including J_{SC}, FF, and PCE [46–48]. The influence of CBO on V_{OC} can be mathematically described using following Equations [49]

$$V_{oc} = \frac{E_A}{q} - \frac{nkT}{q} \ln \frac{J_{00}}{J_{sc}} \tag{7}$$

$$E_A = E_g - CBO \tag{8}$$

where, n is the diode ideality factor, K stands for the Boltzmann constant, T is the temperature, and J_{00} is the current prefactor.

3.2.4 | Effect of Series Resistance (Rs)

The individual shunt resistance (R_{sh}) and series resistance (R_s) play crucial roles in shaping the current–voltage (J–V) characteristics and significantly impact the performance of PSCs. These resistances primarily arise from layer-to-layer connections, metal contacts, and manufacturing defects, affecting overall solar cell efficiency [50]. To analyze the impact of R_s on PSC performance, R_s was varied from 1 to 6 Ω•cm^2 whereas maintaining R_{sh} at a constant 10^5 Ω•cm^2, as shown in Figure 11a. The results show that the open-circuit voltage (V_{OC}) and short-circuit current density (J_{SC}) remain relatively stable, while the fill factor (FF) decreases significantly as the series resistance (R_s) increases, resulting in a decrease in power conversion efficiency (PCE) for all six structures. The J–V characteristics of a hetero-junction solar cell are typically represented by the diode equation [51]

$$J = J_L - J_0 \left[\exp\left(\frac{q_e (V + JR_s)}{nK_B T} \right) - 1 \right] - \frac{V + JR_s}{R_{sh}} \tag{9}$$

where J is the circuit current, J_L is the photocurrent generated by light absorption, V is the applied voltage, and J_0 is the saturation current in reverse direction.

In a study on $CH_3NH_3SnI_3$-based solar cells, performance was evaluated by adjusting R_s from 0 to 6 Ω•cm^2 while keeping R_{sh} constant at 10^5 Ω•cm^2. The findings revealed that current remains largely unaffected by R_s variations, consistent with the results of Sunny et al. for $R_s \geq 30$ Ω•cm^2 [52]. However, when R_s reaches or exceeds 30 Ω•cm^2, current decreases sharply, as reported by Karthick et al. [53]. Although their study was experimental, it noted that R_s accounts for cumulative resistances across various components, including the absorber, ETL, HTL, and front and back contacts. Series resistance does not significantly impact current until a critical threshold is reached. Simulated results indicate that varying the ETLs does not affect the current of Cs_2AuScI_6 perovskite when R_s surpasses 30 Ω•cm^2. However, experimental studies may yield different outcomes, warranting further investigation. The analysis highlights that increasing R_s reduces both PCE and FF while having minimal effect on J_{SC} and V_{OC} until a specific limit is exceeded. This underscores the importance of reducing R_s through careful material selection and optimized manufacturing techniques to achieve high-efficiency PSCs. While simulation results suggest potential optimization strategies, experimental validation is necessary to refine real-world performance.

3.2.5 | Effect of Shunt Resistance (R_{sh})

High R_{sh} is necessary to enhance the efficiency of solar cells, as shunt resistance impacts the photovoltaic properties of DPSCs [54]. The effect of R_{sh} on Cs_2AuScI_6-based solar cells is shown in Figure 11b. In PSCs, power losses are analyzed using shunt resistance and include leakage currents as well as nongeminate recombination. Defects in solar cells, such as pinholes and metal penetration, reduce R_{sh} in practical devices, creating additional pathways for photogenerated current and leading to energy losses. A low R_{sh} reduces the current flow through the junction, especially under low-light conditions, where photogenerated current is lower, making the effects of current loss through shunt resistance more prominent [55]. Furthermore, parallel resistance should be considered at low voltage levels, as this increases the solar cell's effective resistance. These factors underscore the need to fine-tune R_{sh} to the highest possible value, thereby minimizing power losses and enhancing overall device performance [56]. Analyzing the R_{sh} factor from 10 to 10^6 Ω•cm^2 reveals its impact on the photovoltaic performance of the ITO/ETL/Cs_2AuScI_6/CBTS/Ni device. The graph illustrates significant variations in V_{OC}, J_{SC}, FF, and PCE in response to changes in R_{sh}. Increasing R_{sh} from 10 to 10^2 Ω•cm^2 results in a significant PCE increase from 2.5% to ∼20%. Beyond 10^2 Ω•cm^2, device performance improves slightly, reaching a maximum efficiency of ∼26% at 10^3 Ω•cm^2, stabilizing thereafter for materials like WS_2, ZnO, TiO_2, PCBM, and IGZO. C_{60} exhibits the highest PCE (∼18%) beyond 10^3 Ω•cm^2 before stabilizing. Variations in R_{sh} are linked to fabrication defects, which create low-resistance pathways. Higher R_{sh} values minimize these effects and improve device performance. V_{OC} increases as R_{sh} rises, reaching an optimal value at 10^3 Ω•cm^2, while J_{SC} remains relatively stable, aligning with experimental results from previous studies. Without C_{60}, all studied devices exhibit similar trends. Thus, maintaining an R_{sh} of 10^3 Ω•cm^2 or higher is crucial for achieving maximum PCE in ITO/ETL/Cs_2AuScI_6/CBTS/Ni solar cells.

3.2.6 | Effect of Temperature

The operating temperature significantly impacts the performance of solar cells such as CIGS [57]. Variations in temperature affect the overall efficiency and operational parameters of these devices. In particular, the effects of temperature on the photovoltaic (PV) parameters, including PCE, short-circuit current density (J_{SC}), open-circuit voltage (V_{OC}), and fill factor (FF), for the ITO/ETL/Cs_2ScAuI_6/CBTS/Ni hetero-junction DPSC, are shown in Figure 12, with temperatures going from 300 to 425 K. The relationship between temperature and PV characteristics is well-established in conventional semiconductors. Among the

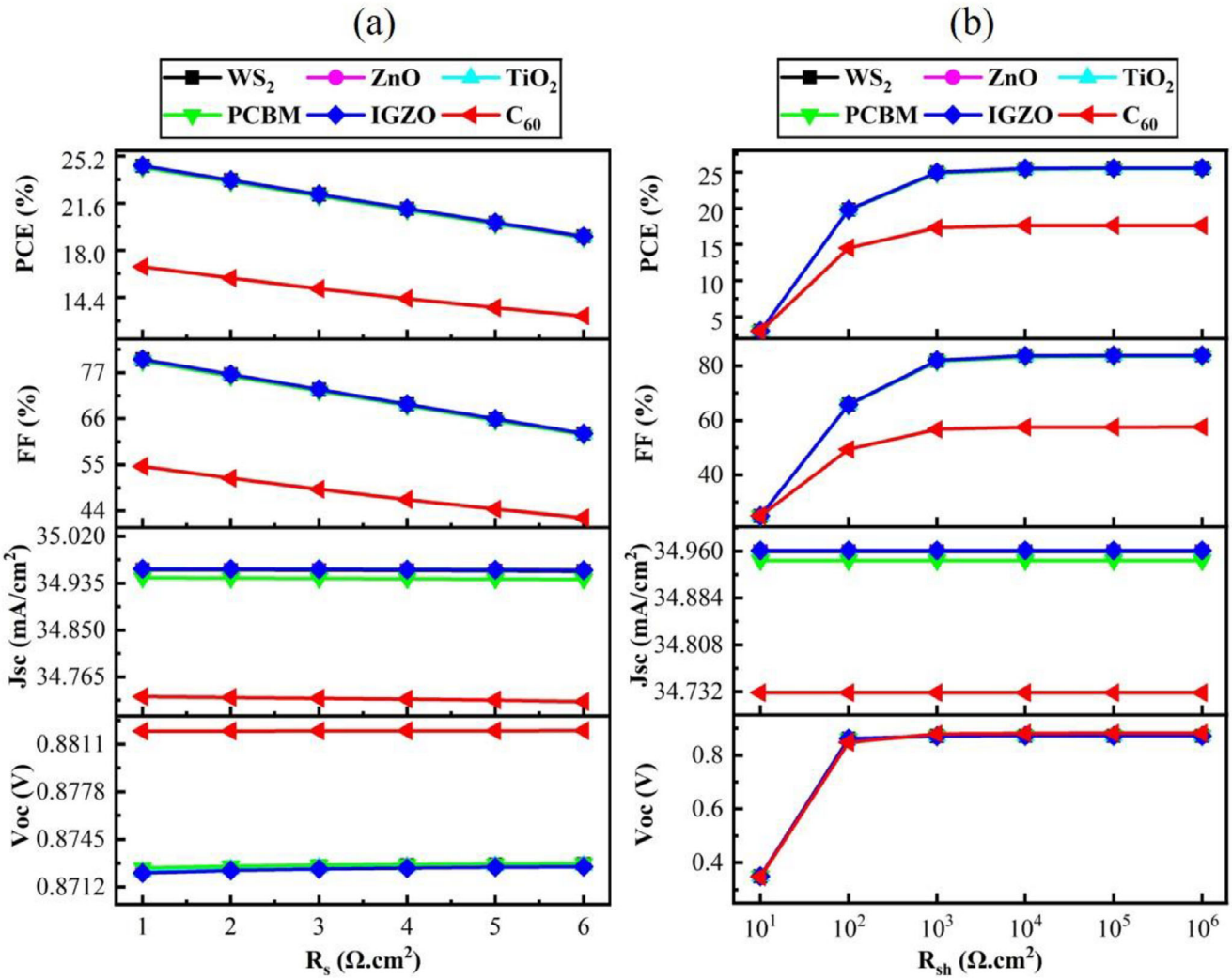

FIGURE 11 | Effect of photovoltaic performance parameters (V_{oc}, J_{sc}, FF, and PCE) for (a) series (R_s) and (b) shunt resistances (R_{sh}).

parameters, V_{OC} is the most sensitive to temperature increases, as shown in Figure 12a. As temperature rises, the saturation current density (J_0) increases significantly due to an enhanced recombination rate, which occurs because of changes in intrinsic carrier concentrations. The inverse correlation between V_{OC} and J_0 accounts for the reduction in V_{OC}, which decreases from 0.90 to 0.65 V across all analyzed device configurations. Consequently, FF decreases from approximately 84% to 74% for most optimal configurations, except those using C_{60} as the ETL layer. All device structures experience a decline in V_{OC}, FF, and PCE with increasing temperature. Conversely, J_{SC}, shown in Figure 12b, changes only slightly with temperature, as the bandgap undergoes only a slight decrease. This suggests that temperature has a minimal effect on J_{SC}, which is consistent with the behavior of double perovskites that exhibit nearly constant bandgap values. When comparing the ETL materials, devices with IGZO show a higher J_{SC} (~35 mA/cm^2), while those using C_{60} display the lowest value (~34.3 mA/cm^2). This discrepancy implies that the choice of ETL material influences device performance [58]. Although J_{SC} remains relatively stable across all device configurations, both PCE and V_{OC}, as well as FF, decrease with rising temperature. Additionally, defect-related effects worsen at higher temperatures, further degrading V_{OC}. The findings of this study align with previous research, which consistently highlights that the primary causes of efficiency degradation in solar cells under elevated temperatures are recombination effects and inherent limitations resulting from changes in the bandgap [50].

3.2.7 | Effects of Capacitance Voltage (C–V), Mott–Schottky (M–S) Plot Analysis, Generation, and Recombination Rates

Figure 13a,b shows the capacitance voltage (C–V) and Mott–Schottky characteristics of solar cells made of Cs_2AuScI_6 with different ETL options, all measured at a constant frequency of 1 MHz. In all the devices examined, the capacitance rises as the voltage is applied within the range of −0.8 to 0.8 V. In Figure 13a, the capacitance is almost constant for the negative supply voltage. Then the capacitance increases exponentially with an increase in supply voltage. The C_{60} based device shows the most capacity, at 0.8 V, is 52.5 nF/cm^2, indicating a charge buildup at the connection point interface. However, other devices indicate lower capacity, hinting at a depletion area and less effective carrier retrieval. When no bias is applied, all devices operate in depletion mode, resulting in reduced capacitance. As the forward bias

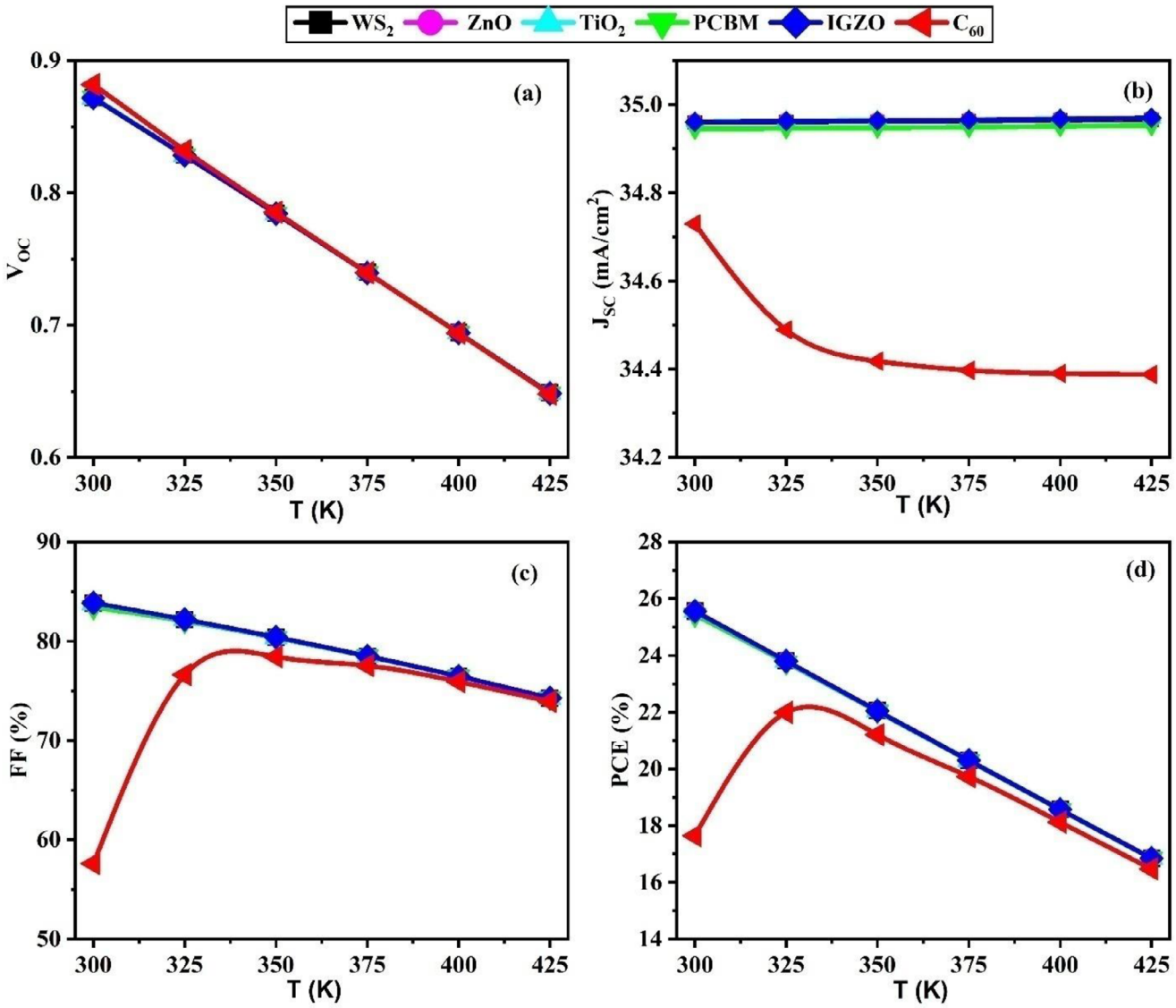

FIGURE 12 | Effect of temperature on performance parameters (a) V_{oc}, (b) J_{sc}, (c) FF, and (d) PCE of (ITO/ETL/Cs_2ScAuI_6/CBTS/Ni) when ETL = WS_2, ZnO, TiO_2, PCBM, IGZO, and C_{60}.

voltage rises, the depletion zone reduces, leading to an increase in capacitance. The pattern aligns with how perovskite solar cells behave when the applied voltage affects the distribution of electric charge across the junction area. By looking at Figure 13b, we can see how the built-in potential (known as V_{bi}) distinguishes between the activities of electrode operation and the level of dopants, which is calculated by the Mott–Schottky method [59–60]. The following equation provides the junction capacitance per unit area (C) and is applicable to traditional semiconductor devices that include p–n junctions and semiconductor junctions with fixed depletion layers and space charge regions [61]

$$\frac{1}{c^2} = \frac{2\varepsilon_0\varepsilon_r}{qN_d}(V_{bi} - V) \tag{10}$$

Here, ε_0 represents the vacuum permittivity, ε_r denotes the dielectric constant of the donor, q is the electronic charge, and V refers to the applied voltage.

Figure 13c,d displays the rates of carrier generation and recombination throughout the depth of the absorbing layer. What's noteworthy is that the rate of generation ($G(x)$) reaches its peak around a thickness of 1.0–1.1 μm for all devices. This indicates optimal photon absorption and electron–hole pair generation in this region due to the high optical absorption coefficient of the Cs_2AuScI_6 absorber material. Among the ETLs, IGZO, and ZnO exhibit slightly higher generation rates compared to PCBM and TiO_2, signifying better photon management and reduced reflection losses. The generation rate is calculated using the SCAPS-1D framework, based on the photon flux ($N_{phot}(\lambda, x)$) and the absorption coefficient ($\alpha(\lambda,x)$), as expressed in equation below [23]

$$G(\lambda, x) = \alpha(\lambda, x) N_{phot}(\lambda, x) \tag{11}$$

This equation captures the spatial and spectral dependence of photon absorption across the device. The recombination rate exhibits a distinct peak near the same region (1.0–1.1 μm),

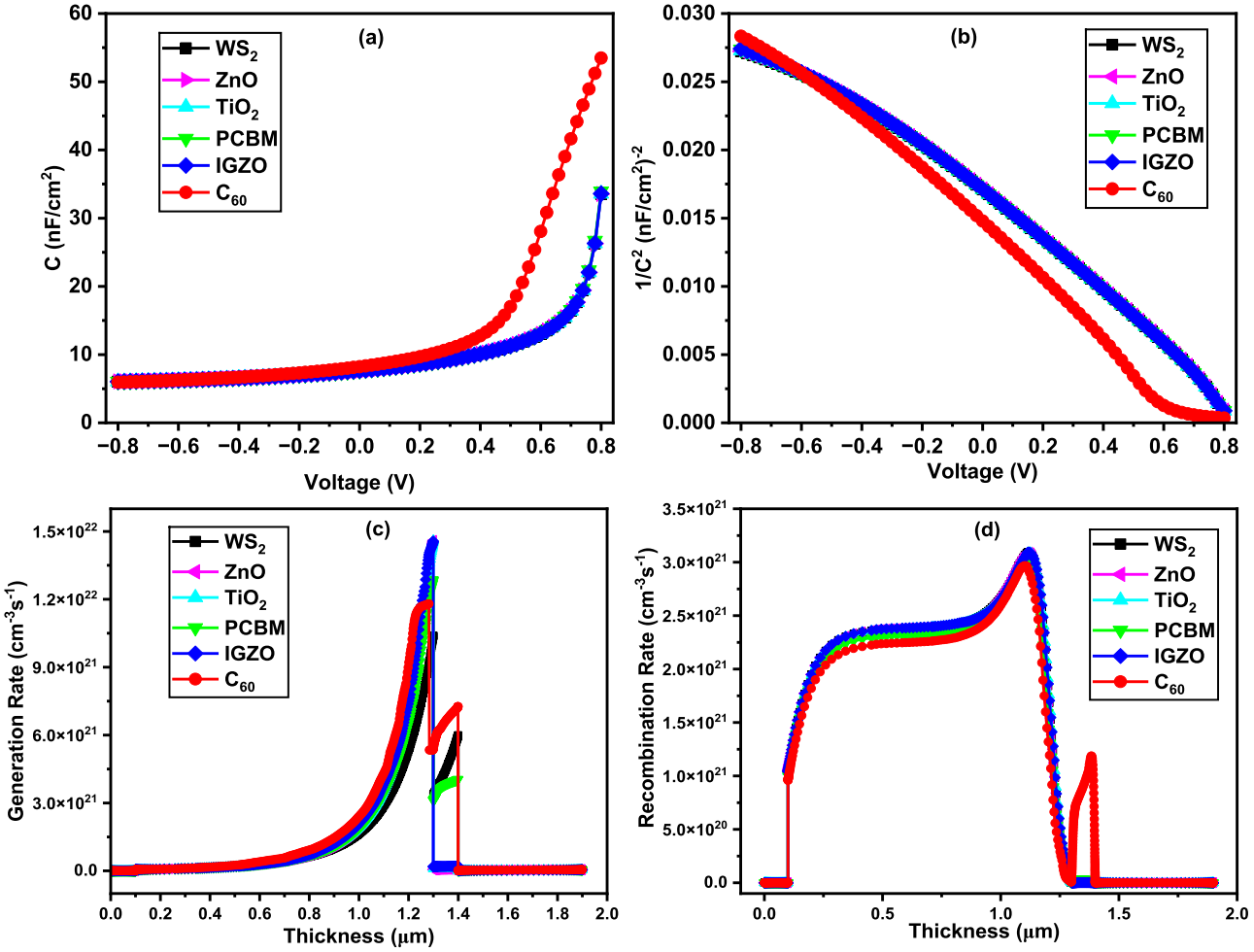

FIGURE 13 | Effects of (a) Capacitance (C), (b) Mott–Scottky plot ($1/C^2$), (c) Generation rate, and (d) Recombination rate for six ETL structures.

reflecting the interplay between carrier generation and loss mechanisms. All devices exhibit the highest recombination peak, indicating higher defect densities and carrier trapping states in the interface and bulk regions, except for C_{60}. C_{60}-based devices exhibit lower recombination rates, which is attributed to their superior passivation properties and longer carrier lifetimes. Recombination within the perovskite absorber is primarily governed by Shockley–Read–Hall (SRH) mechanisms at defect sites [62]. The mid-gap states act as recombination centers, where trapped carriers annihilate [49].

3.2.8 | Effect of Acceptor Density

The performance of PSCs is enhanced by optimizing the absorber layer. Changes to the acceptor density of the absorber layer influence how well a photovoltaic device performs, as shown in Figure 14. In this analysis, six ETL materials (WS_2, ZnO, TiO_2, PCBM, IGZO, and C_{60}) were tested by adjusting acceptor density (N_A) levels from 10^{13} to 10^{18} cm^{-3} to achieve top performance for every configuration. It is observed that a high doping value increases Auger recombination [63]. Impurities are introduced by doping the absorber layer, resulting in electron deficits or "holes" in the semiconductor material that serve as majority charge carriers. The mobility of charge carriers is improved when

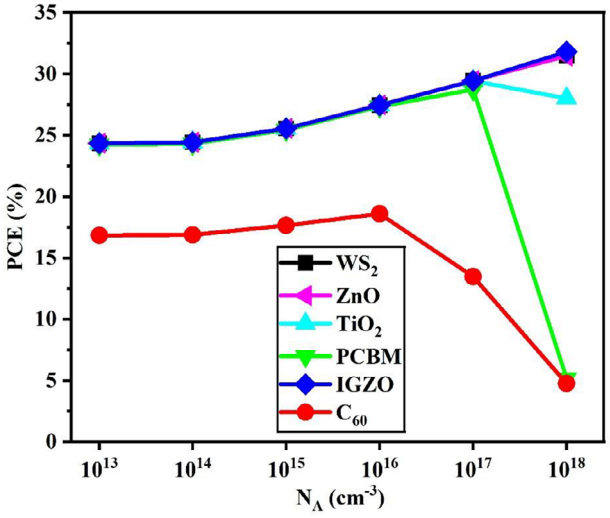

FIGURE 14 | Acceptor density optimization with different ETLs for Cs_2AuScI_6 compound.

the doping concentration rises because there are more accessible holes. Our findings showed that as the doping concentration rises, so does the short-circuit current density. The intrinsic electric field across the device increases as the doping concentration

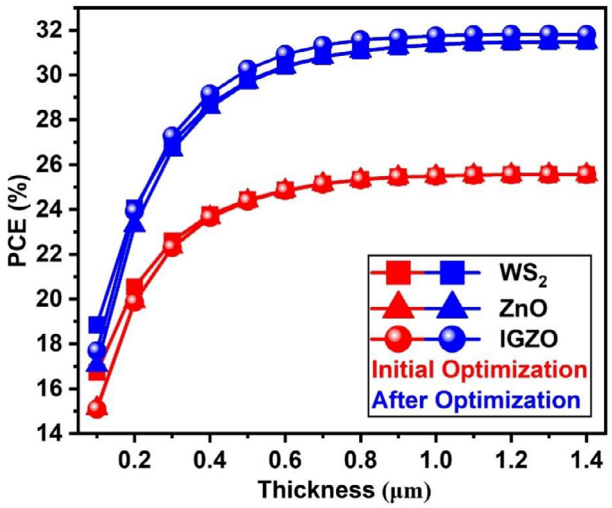

FIGURE 15 | Absorber thickness optimization with best ETLs (Ws_2, ZnO, and IGZO).

rises from 10^{13}, improving the separation of the photogenerated carriers and raising the V_{OC} and cell efficiency. If the double halide perovskite is aimed at solar cell applications, typical N_A values often lie in the range of 10^{15}–10^{18} cm^{-3} to match reported doping concentrations [9], [64–67]. The peak PCE is observed as follows for the ETLs: WS_2: 31.48% at 10^{18} cm^{-3}, ZnO: 31.46% at 10^{18} cm^{-3}, TiO_2: 29.44% at 10^{17} cm^{-3}, PCBM: 28.75% at 10^{17} cm^{-3}, IGZO: 31.82% at 10^{18} cm^{-3}, and C_{60}: 18.61% at 10^{16} cm^{-3}. WS_2, ZnO, and IGZO are the top performers among them. Charge generation and extraction improve moderately when acceptor density increases, but higher levels amplify recombination issues.

3.2.9 | Effect of Absorber Thickness

The optimization of the absorber layer thickness was investigated by varying its value from 0.1 to 1.4 μm, as shown in Figure 15. The study utilized WS_2, ZnO, and IGZO as the best ETL by analyzing acceptor density, with results presented both before and after optimization. At lower thickness, the efficiency increases sharply as the thickness of the absorber rises. This is because, at very thin absorber layers (0.1–0.3 μm), the material may not be able to absorb enough sunlight to generate a significant amount of charge carriers (electrons and holes). As the thickness increases (from 0.3 μm to above), the absorber can capture more photons, leading to more generation of charge carriers and thus more current, which boosts the efficiency [68]. After a certain thickness, the efficiency tends to plateau. This suggests that there is an optimal thickness beyond which increasing the thickness does not significantly enhance efficiency. At these thicknesses, the absorber layer is thick enough to absorb a substantial portion of the incident light, leading to a near-maximal generation of charge carriers. The plateau indicates that the solar cells are efficiently converting most of the absorbed light into electrical energy. Additionally, in thicker layers, charge carriers may have to travel longer distances to reach the electrodes, thereby increasing the possibility of recombination before they contribute to current flow. However, the efficiency either plateaus or remains nearly constant (0.5–1.4 μm) in this study, suggesting that the materials are well-optimized to minimize such losses at the given thickness range.

3.2.10 | Current Density vs. Voltage (*J–V*) and Quantum Efficiency (QE) Curve

The *J–V* curve and QE for the structure of ITO/ETL/Cs_2ScAuI_6/CBTS/Ni, employing high-performance ETLs such as WS_2, ZnO, and IGZO, are illustrated in Figure 16. The initial and optimized *J–V* curves are shown in Figure 16a. All three ETLs exhibit nearly identical values in the *J–V* curve, indicating the same photogenerated current across the devices for each investigated ETL. Variations occur occasionally due to the band structure of the ETLs. If defects are present in perovskite films, there is a notable decline in the performance of all photovoltaic films. These results support the idea that perovskite solar structures with a high level of crystallinity help reduce charge recombination and enhance efficiency [69]. The QE curve of the devices as a function of light wavelength is shown in Figure 16b. The wavelength range of 200–1100 nm is used to assess the suitability of the devices. From this data, it is clear that QE increases with wavelength due to more absorbing photons [70], reaching 100% when the wavelength is equal to or greater than 360 nm. The QE then gradually decreases to zero as the wavelength approaches 900 nm. As observed from the *J–V* characteristics, the WS_2, ZnO, and IGZO devices exhibit similar QE behavior due to precise optimization.

3.2.11 | Comparison with Other Works

Figure 17 presents a theoretical photovoltaic study of the materials in question, comparing their performance with other similar absorber materials. Although there are no prior studies specifically focused on these materials, comparable research has been conducted on analogous double halide compounds for energy harvesting. Notably, studies on Cs_2BiAgI_6 and $Cs_2AgBiBr_6$ have shown significant improvements in PCE, reaching 21.59% and 23.50%, respectively.

In this study, various ETL configurations were evaluated. Among the structures tested—ITO/WS_2/Cs_2AuScI_6/CBTS/Ni, ITO/ZnO/Cs_2AuScI_6/CBTS/Ni, ITO/TiO_2/Cs_2AuScI_6/CBTS/Ni, ITO/PCBM/Cs_2AuScI_6/CBTS/Ni, and ITO/IGZO/Cs_2AuScI_6/CBTS/Ni—several demonstrated significant potential for energy conversion applications, with efficiencies of 31.48%, 31.46%, 29.44%, 28.75%, and 31.82%, respectively. The enhanced efficiency of the Cs_2AuScI_6-based solar cells with CBTS as HTL is attributed to multiple aspects. CBTS exhibits excellent energy level alignment with Cs_2AuScI_6 absorber, which is beneficial to effectively modulate charge transport and recombination. Its excellent mobility and low defect density reduce the recombination losses on the interface. Moreover, CBTS exhibits superior stability and Cs_2AuScI_6 compatibility over conventional HTL PEDOT:PSS, resulting in enhanced device performance. This research highlights the enhanced efficiency and photovoltaic performance achieved, surpassing the results of previous studies. While all five devices exhibit notable PCE improvements compared to earlier

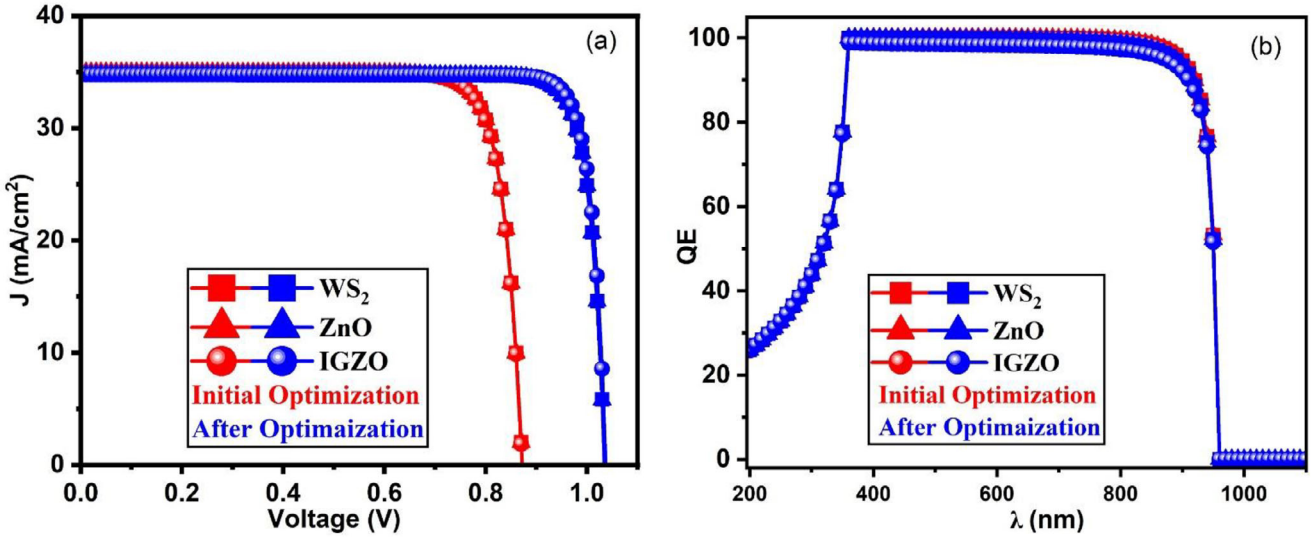

FIGURE 16 | (a) *J–V* characteristics and (b) QE curve of the Cs_2AuScI_6 based-PSC.

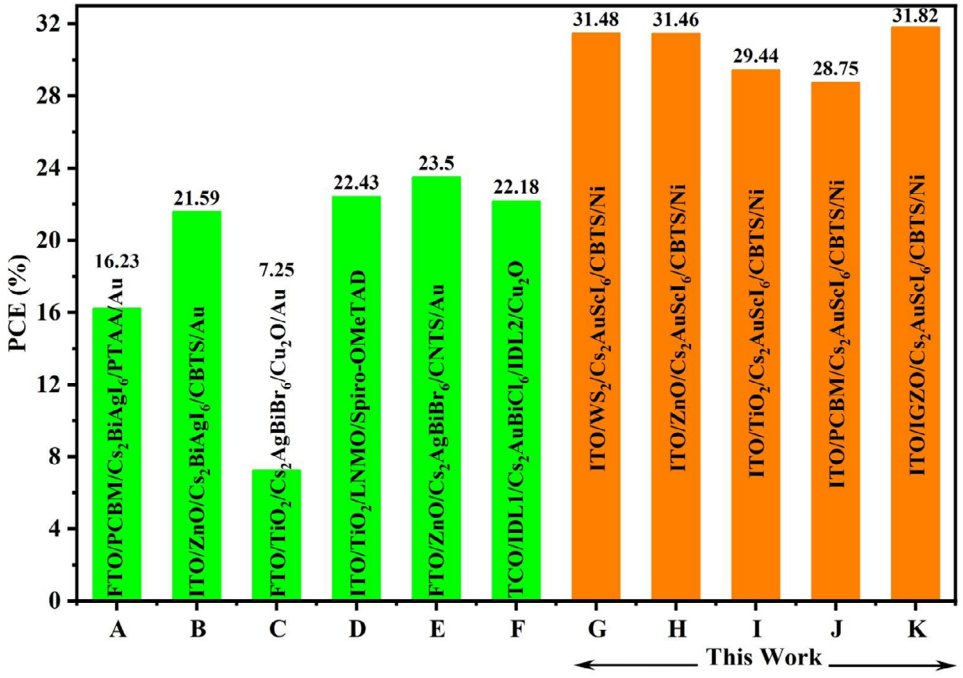

FIGURE 17 | Comparison of the theoretical study with other similar types of absorber materials (A = [71], B = [44], C = [72], D = [73], E = [21], F = [24]).

theoretical investigations, the ITO/IGZO/Cs_2AuScI_6/CBTS/Ni device stands out with exceptional performance across the board. As a result, the proposed solar cell framework—developed through SCAPS-1D simulations and DFT computations—provides a novel pathway for achieving higher-efficiency devices in the future.

4 | Conclusion

This research thoroughly investigates the potential of Cs_2AuScI_6, a double halide perovskite material, as a lead-free and environmentally friendly alternative for photovoltaic systems. By utilizing DFT and SCAPS-1D simulations, we conducted a detailed analysis of the material's structural, electronic, and optoelectronic properties, as well as its performance within solar cell configurations. Structurally, the material validates excellent stability in its cubic phase, as indicated by its tolerance factor and octahedral factor, suggesting that it is a viable candidate for experimental synthesis. From the electronic point of view, Cs_2AuScI_6 has an indirect bandgap of 1.30 eV, which is ideal for photovoltaic applications, allowing for efficient photon absorption in the visible spectrum and improving its light-capturing capacity. Optical analysis further reveals that the material has a high absorption coefficient and low reflectance in the visible range, making it well-suited for use as an absorber layer in solar

devices. SCAPS-1D simulations provided usable insights into the material's performance in various solar cell configurations. Among the different device architectures, the configuration with Cs_2AuScI_6 as the absorber layer and CBTS as the HTL showed the best performance. Devices using different ETLs, such as WS_2, ZnO, TiO_2, PCBM, and IGZO, yielded notable PCEs of 25.58%, 25.58%, 25.57%, 25.45%, and 25.58%, respectively, in initial optimization. Additionally, parametric studies were conducted to assess the influence of key factors like absorber thickness, acceptor doping density, series and shunt resistances, and temperature. Optimizing the acceptor doping density resulted in maximum efficiencies of 31.48%, 31.46%, 29.44%, 28.75%, and 31.82% for the five ETL configurations (WS_2, ZnO, TiO_2, PCBM, and IGZO) in the ITO/ETL/Cs_2AuScI_6/CBTS/Ni device structure.

In conclusion, Cs_2AuScI_6 shows great promise as a lead-free material for efficient and sustainable photovoltaic applications. Its exceptional structural stability, favorable optoelectronic properties, and high simulated device efficiency make it a viable alternative to lead-based perovskites. This research contributes to the ongoing effort to develop sustainable solar technologies that can help address climate change and facilitate the global transition to renewable energy sources.

Author Contributions

S.M. contributed to writing the original draft, methodology, conceptualization, formal analysis, data calculations, and validation. M.M.I. contributed to writing, reviewing, editing, investigation, and validation. M.M.H. contributed to writing, reviewing, editing, and validation. M.M.U. contributed to writing, reviewing, editing, and validation. M.A.A. contributed to conceptualization, formal analysis, validation, writing, reviewing, editing, supervision, and project administration.

Acknowledgements

This work was carried out with the aid of a grant (Grant No. 21-378 RG/PHYS/AS_G -FR3240319526) from UNESCO-TWAS and the Swedish International Development Co-operation Agency (SIDA). The views expressed herein do not necessarily represent those of UNESCO-TWAS, SIDA or its Board of Governors. S. Mahmud expresses gratitude to the University Grants Commission (UGC) of Bangladesh for providing financial support to conduct this research under Ph.D. Fellowship program 2022–2023.

Conflicts of Interest

The authors declare that they have no known competing financial interests or personal relationships that could have appeared to influence the work reported in this paper.

Data Availability Statement

The datasets used and/or analyzed during the current study available from the corresponding author on reasonable request.

References

1. L. L. Brunton, R. Hilal-Dandan, and B. C. Knollmann, Goodman & Gilman's *T*he Pharmacological Basis of Therapeutics (McGraw-Hill Education, NY, USA 2017).

2. M. Mammeri, L. Dehimi, H. Bencherif, et al., "Targeting High Performance of Perovskite Solar Cells by Combining Electronic, Manufacturing and Environmental Features in Machine Learning Techniques," *Heliyon* 9, no. 11 (2023): 21498.

3. P. Gao, M. Grätzel, and M. K. Nazeeruddin, "Organohalide Lead Perovskites for Photovoltaic Applications," *Energy & Environmental Science* 7, no. 8 (2014): 2448–2463.

4. J. Jeong, M. Kim, J. Seo, et al., "Pseudo-Halide Anion Engineering for α-$FAPbI_3$ Perovskite Solar Cells," *Nature* 592, no. 7854 (2021): 381–385.

5. S. Murugan and E.-C. Lee, "Recent Advances in the Synthesis and Application of Vacancy-Ordered Halide Double Perovskite Materials for Solar Cells: A Promising Alternative to Lead-Based Perovskites," *Materials* 16, no. 15 (2023): 5275.

6. A. S. Thind, S. Kavadiya, M. Kouhnavard, et al., "$KBaTeBiO_6$: A Lead-Free, Inorganic Double-Perovskite Semiconductor for Photovoltaic Applications," *Chemistry of Materials* 31, no. 13 (2019): 4769–4778.

7. M. Pantaler, K. T. Cho, V. I. E. Queloz, et al., "Hysteresis-Free Lead-Free Double-Perovskite Solar Cells by Interface Engineering," *ACS Energy Letters* 3, no. 8 (2018): 1781–1786.

8. X. Cui, Y. Li, N. Sun, et al., "Double Perovskite $Bi_2FeMoNi_{1-x}O_6$ Thin Films: Novel Ferroelectric Photovoltaic Materials with Narrow Bandgap and Enhanced Photovoltaic Performance," *Solar Energy Materials and Solar Cells* 187 (2018): 9–14.

9. N. Singh, A. Agarwal, and M. Agarwal, "Performance Evaluation of Lead–Free Double-Perovskite Solar Cell," *Optical Materials* 114 (2021): 110964.

10. M. Roknuzzaman, C. Zhang, K. Ostrikov, et al., "Electronic and Optical Properties of Lead-Free Hybrid Double Perovskites for Photovoltaic and Optoelectronic Applications," *Scientific Reports* 9, no. 1 (2019): 718.

11. G. Meng, N. K. Elumalai, H. Mehdizadeh-Rad, K. S. Ram, D. D. Y. Setsoafia, and D. Ompong, "Investigating the Impact of Interfacial Layers on Device Performance of Highly Stable $Cs_2InBiBr_6$ Based Double Perovskite Solar Cells," *Advanced Theory and Simulations* 7, no. 2 (2024): 2300784.

12. M. Usman and Q. Yan, "Recent Advancements in Crystalline Pb-Free Halide Double Perovskites," *Crystals* 10, no. 2 (2020): 62.

13. W. Ke and M. G. Kanatzidis, "Prospects for Low-Toxicity Lead-Free Perovskite Solar Cells," *Nature Communications* 10, no. 1 (2019): 965.

14. M. Sajjad, Q. Mahmood, N. Singh, and J. A. Larsson, "Ultralow Lattice Thermal Conductivity in Double Perovskite Cs_2PtI_6: A Promising Thermoelectric Material," *ACS Applied Energy Materials* 3, no. 11 (2020): 11293–11299.

15. S. Yun, X. Zhou, J. Even, and A. Hagfeldt, "Theoretical Treatment of $CH_3NH_3PbI_3$ Perovskite Solar Cells," *Angewandte Chemie International Edition* 56, no. 50 (2017): 15806–15817.

16. M. Sk, G. Gourav, and S. Ghosh, "Ab Initio Study of Structural, Electronic, Optical, and Thermoelectric Properties of $Cs_2(Li/Na)GaI_6$ for Green Energy Applications," *Physica Status Solidi (b)* 262, no. 1 (2025): 2400263.

17. M. S. Gourav, K. Ramachandran, and S. Ghosh, "First-Principles Investigation of Rb_2Ag (Ga/In)Br_6 for Thermoelectric and Photovoltaic Applications," *International Journal of Quantum Chemistry* 122, no. 14 (2022): 26910.

18. M. Sk and S. Ghosh, "First-Principles Investigation of Structural, Optoelectronic, and Thermoelectric Properties of $Cs_2Tl(As/Sb)I_6$, Optoelectronic, and Thermoelectric Properties of $Cs_2Tl(As/Sb)I_6$," *International Journal of Energy Research* 46, no. 8 (2022): 10553–10563.

19. M. Sk and K. Ramachandran, "First-Principles Investigation of $Rb_2Tl(As/Bi)I_6$ for Green Technology," *Chemical Physics Impact* 4 (2022): 100071.

20. H. Sabbah, Z. Abdel Baki, R. Mezher, and J. Arayro, "SCAPS-1D Modeling of Hydrogenated Lead-Free $Cs_2AgBiBr_6$ Double Perovskite Solar Cells with a Remarkable Efficiency of 26.3%," *Nanomaterials* 14, no. 1 (2023): 48.

21. M. S. Uddin, M. K. Hossain, M. B. Uddin, et al., "An In-Depth Investigation of the Combined Optoelectronic and Photovoltaic Properties of

Lead-Free $Cs_2AgBiBr_6$ Double Perovskite Solar Cells Using DFT and SCAPS-1D Frameworks," *Advanced Electronic Materials* 10, no. 5 (2024): 2300751.

22. X. Yang, W. Wang, R. Ran, W. Zhou, and Z. Shao, "Recent Advances in $Cs_2AgBiBr_6$-Based Halide Double Perovskites as Lead-Free and Inorganic Light Absorbers for Perovskite Solar Cells," *Energy & Fuels* 34, no. 9 (2020): 10513–10528.

23. K. I. Ferdous Utsho, S. M. G. Mostafa, M. Tarekuzzaman, et al., "Optimizing $Cs_2CuBiBr_6$ Double Halide Perovskite for Solar Applications: The Role of Electron Transport Layers in SCAPS-1D Simulations," *RSC Advances* 15, no. 3 (2025): 2184–2204.

24. A. J. Kale, R. Chaurasiya, and A. Dixit, "Inorganic Lead-Free $Cs_2AuBiCl_6$ Perovskite Absorber and Cu_2O Hole Transport Material Based Single-Junction Solar Cells with 22.18% Power Conversion Efficiency," *Advanced Theory and Simulations* 4, no. 3 (2021): 2000224.

25. Y. El Arfaoui, M. Khenfouch, and N. Habiballah, "HTL-free Non-Toxic Perovskite Tandem Solar Device $MAGeI_3/FASnI_3$ with 25.69% Efficiency: Design and Simulation Using SCAPS," *Journal of Optics* 53, no. 5 (2024): 4452–4465.

26. Y. El Arfaoui, M. Khenfouch, and N. Habiballah, "DFT and SCAPS-1D Calculations of $FASnI_3$-Based Perovskite Solar Cell Using ZnO as an Electron Transport Layer," *The European Physical Journal Applied Physics* 98 (2023): 60.

27. Y. El Arfaoui, M. Khenfouch, and N. Habiballah, "Optimization of all Pb-Free Perovskite $CsGeI_3/FASnI_3$ Tandem Solar Device with 30.42% Efficiency: Numerical Simulation Using SCAPS," *Optik* 300 (2024): 171638.

28. Y. El Arfaoui, M. Khenfouch, and N. Habiballah, "Efficient all Lead-Free Perovskite Solar Cell Simulation of $FASnI_3/FAGeCl_3$ with 30% Efficiency: SCAPS-1D Investigation," *Results in Optics* 13 (2023): 100554.

29. M. K. Chini, S. G. Srinivasan, N. K. Tailor, D. Salahub, and S. Satapathi, "Lead-Free, Stable Mixed Halide Double Perovskites $Cs_2AgBiBr_6$ and $Cs_2AgBiBr_{6-x}Cl_x$ – A Detailed Theoretical and Experimental Study," *Chemical Physics* 529 (2020): 110547.

30. A. Bhorde, R. Waykar, S. R. Rondiya, et al., "Structural, Electronic, and Optical Properties of Lead-Free Halide Double Perovskite Rb_2AgBiI_6: A Combined Experimental and DFT Study," *ES Materials & Manufacturing* 12 (2021): 43–52.

31. K. Schwarz, "DFT Calculations of Solids with LAPW and WIEN2k," *Journal of Solid State Chemistry* 176, no. 2 (2003): 319–328.

32. J. P. Perdew, K. Burke, and M. Ernzerhof, "Generalized Gradient Approximation Made Simple," *Physical Review Letters* 77, no. 18 (1996): 3865.

33. F. Tran and P. Blaha, "Accurate Band Gaps of Semiconductors and Insulators with a Semilocal Exchange-Correlation Potential," *Physical Review Letters* 102, no. 22 (2009): 226401.

34. S. S. Hussain, S. Riaz, G. A. Nowsherwan, et al., "Numerical Modeling and Optimization of Lead-Free Hybrid Double Perovskite Solar Cell by Using SCAPS-1D," *Journal of Renewable Energy* 2021, no. 1 (2021): 6668687.

35. F. Liu, J. Zhu, J. Wei, et al., "Numerical Simulation: Toward the Design of High-Efficiency Planar Perovskite Solar Cells," *Applied Physics Letters* 104, no. 25 (2014).

36. S. Mahmud, M. A. Ali, M. M. Hossain, and M. M. Uddin, "DFT Aided Prediction of Phase Stability, Optoelectronic and Thermoelectric Properties of A_2AuScX_6 (A = Cs, Rb; X = Cl, Br, I) Double Perovskites for Energy Harvesting Technology," *Vacuum* 221 (2023): 112926.

37. M. Sk and S. Ghosh, "16.35 % Efficient $Cs_2GeSnCl_6$ Based Heterojunction Solar Cell with Hole-Blocking SnO_2 Layer: DFT and SCAPS-1D Simulation," *Optik* 267 (2022): 169608.

38. S. Mahmud, U. Ahmed, M. A. U. Z. Atik, M. M. Hossain, M. M. Uddin, and M. A. Ali, "Novel $Cs_2Au^{I}M^{III}F_6$ (M = As, Sb) Double Halide Perovskites: Sunlight and Industrial Waste Heat Management Device Applications," *Physical Chemistry Chemical Physics* 27 (2025): 4686–4703.

39. Y. Zhou and G. Long, "Low Density of Conduction and Valence Band States Contribute to the High Open-Circuit Voltage in Perovskite Solar Cells," *The Journal of Physical Chemistry C* 121, no. 3 (2017): 1455–1462.

40. S. Mahmud, M. M. Hossain, M. M. Uddin, and M. A. Ali, "Prediction of X_2AuYZ_6 (X = Cs, Rb; Z = Cl, Br, I) Double Halide Perovskites for Photovoltaic and Wasted Heat Management Device Applications," *Journal of Physics and Chemistry of Solids* 196 (2025): 112298.

41. H. Pan, X. Zhao, X. Gong, et al., "Advances in Design Engineering and Merits of Electron Transporting Layers in Perovskite Solar Cells," *Materials Horizons* 7, no. 9 (2020): 2276–2291.

42. M. Sk and M. T. Islam, "Exploring the Structural, Electronic, Optical, Transport, and Photovoltaic Properties of $Rb_2LiGa(Br/I)_6$ Using DFT and SCAPS-1D Simulations," *Scientific Reports* 14, no. 1 (2024): 24813.

43. J. Xie, F. Liu, and K. Yan, "Perovskite Solar Cells Processed by Solution Nanotechnology," in *Advanced Nanomaterials for Solar Cells and Light Emitting Diodes*, ed. F. Gao (Elsevier, 2019), 119–174.

44. M. K. Hossain, A. A. Arnab, R. C. Das, et al., "Combined DFT, SCAPS-1D, and wxAMPS Frameworks for Design Optimization of Efficient Cs_2BiAgI_6-Based Perovskite Solar Cells with Different Charge Transport Layers," *RSC Advances* 12, no. 54 (2022): 34850–34873.

45. Y. Raoui, H. Ez-Zahraouy, S. Kazim, and S. Ahmad, "Energy Level Engineering of Charge Selective Contact and Halide Perovskite by Modulating Band Offset: Mechanistic Insights," *Journal of Energy Chemistry* 54 (2021): 822–829.

46. P. Lin, L. Lin, J. Yu, S. Cheng, P. Lu, and Q. Zheng, "Numerical Simulation of Cu_2ZnSnS_4 Based Solar Cells with In_2S_3 Buffer Layers by SCAPS-1D," *Journal of Applied Science and Engineering* 17, no. 4 (2014): 383–390.

47. K. Sobayel, K. S. Rahman, M. R. Karim, M. O. Aijaz, M. A. Dar, M. A. Shar, H. Misran, and N. Amin, "Numerical Modeling on Prospective Buffer Layers for Tungsten Di-Sulfide (Ws_2) Solar Cells by Scaps-1d," *Chalcogenide Letters* 15, no. 6 (2018).

48. M. A. Monnaf, A. K. M. M. Haque, M. H. Ali, S. Bhattarai, M. D. Haque, and M. F. Rahman, "Design and Simulation of Cu_2SnSe_3-Based Solar Cells Using Various Hole Transport Layer (HTL) for Performance Efficiency above 32%," *Physica Scripta* 98, no. 12 (2023): 125903.

49. K. Sekar and S. Mayarambakam, "Effect of Annealed and Non-Annealed Inorganic MnS Hole-Transport Layer for Efficient $Sb_2(S,Se)_3$ Solar Cells: A Theoretical Justification," *Physica Status Solidi (b)* 260, no. 6 (2023): 2300087.

50. M. K. Hossain, M. H. K. Rubel, G. F. I. Toki, I. Alam, M. F. Rahman, and H. Bencherif, "Effect of Various Electron and Hole Transport Layers on the Performance of $CsPbI_3$-Based Perovskite Solar Cells: A Numerical Investigation in DFT, SCAPS-1D, and wxAMPS Frameworks," *ACS Omega* 7, no. 47 (2022): 43210–43230.

51. D. K. Maram, H. Abnavi, H. Habibiyan, H. Ghafoorifard, and O. Shekoofa, "TDMA Based Numerical Approach on Modeling of Charge Carrier Transport and Ion Vacancy Motion in Perovskite Solar Cells," in *2020 28th Iranian Conference on Electrical Engineering (ICEE)*, (ICEE, Tabriz, Iran 2020), 1–7, https://doi.org/10.1109/ICEE50131.2020.9260762.

52. E. Bi, W. Tang, H. Chen, et al., "Efficient Perovskite Solar Cell Modules with High Stability Enabled by Iodide Diffusion Barriers," *Joule* 3, no. 11 (2019): 2748–2760.

53. S. Karthick, S. Velumani, and J. Bouclé, "Experimental and SCAPS Simulated Formamidinium Perovskite Solar Cells: A Comparison of Device Performance," *Solar Energy* 205 (2020): 349–357.

54. V. Deswal, S. Kaushik, R. Kundara, and S. Baghel, "Numerical Simulation of Highly Efficient $Cs_2AgInBr_6$-Based Double Perovskite Solar Cell Using SCAPS 1-D," *Materials Science and Engineering: B* 299 (2024): 117041.

55. K. Tvingstedt, L. Gil-Escrig, C. Momblona, et al., "Removing Leakage and Surface Recombination in Planar Perovskite Solar Cells," *ACS Energy Letters* 2, no. 2 (2017): 424–430.

56. M. Kumar, A. Raj, A. Kumar, and A. Anshul, "Theoretical Evidence of High Power Conversion Efficiency in Double Perovskite Solar Cell Device," *Optical Materials* 111 (2021): 110565.

57. A. K. Daoudia, Y. El Hassouani, and A. Benami, "Investigation of the Effect of Thickness, Band Gap and Temperature on the Efficiency of CIGS Solar Cells through SCAPS-1D," *International Journal of Engineering & Technical Research* 6 (2016): 71–75.

58. Y. He, Y. Zhou, Q. Wang, Q. Hao, X. Guo, and S. Li, "Design and Performance Exploration of a Lead-Free All-Inorganic Hydrogenated $Cs_2AgBiBr_6$ -Based Double Perovskite Solar Cell: A Numerical Modeling Study," *Solar RRL* 7, no. 10 (2023): 2300030.

59. M. S. Islam, K. Sobayel, A. Al-Kahtani, M. A. Islam, G. Muhammad, N. Amin, M. Shahiduzzaman, and M. Akhtaruzzaman, "Defect Study and Modelling of SnX_3-Based Perovskite Solar Cells with SCAPS-1D," *Nanomaterials* 11, no. 5 (2021): 1218.

60. G. G. Malliaras, J. R. Salem, P. J. Brock, and C. Scott, "Electrical Characteristics and Efficiency of Single-Layer Organic Light-Emitting Diodes," *Physical Review B* 58, no. 20 (1998): R13411–R13414.

61. Z. Zhang, et al., "Understanding Hole Extraction of Inverted Perovskite Solar Cells," *ACS Applied Materials & Interfaces* 12, no. 50 (2020): 56068–56075.

62. J. Chen and N.-G. Park, "Causes and Solutions of Recombination in Perovskite Solar Cells," *Advanced Materials* 31, no. 47 (2019): 1803019.

63. A. K. Al-Mousoi, M. K. A. Mohammed, A. Kumar, et al., "Understanding Auger Recombination in Perovskite Solar Cells," *Physical Chemistry Chemical Physics* 25, no. 24 (2023): 16459–16468.

64. M. F. Rahman, M. Harun-Or-Rashid, M. R. Islam, et al., "A Deep Analysis and Enhancing Photovoltaic Performance Above 31% with New Inorganic $RbPbI_3$-Based Perovskite Solar Cells via DFT and SCAPS-1D," *Advanced Theory and Simulations* 7, no. 10 (2024): 2400476.

65. S. Khatoon, V. Chakraborty, S. K. Yadav, S. Diwakar, J. Singh, and R. B. Singh, "Simulation Study of $CsPbI_xBr_{1-x}$ and $MAPbI_3$ Heterojunction Solar Cell Using SCAPS-1D," *Solar Energy* 254 (2023): 137–157.

66. B. K. Ravidas, M. K. Roy, and D. P. Samajdar, "Investigation of Photovoltaic Performance of Lead-Free $CsSnI_3$-Based Perovskite Solar Cell with Different Hole Transport Layers: First Principle Calculations and SCAPS-1D Analysis," *Solar Energy* 249 (2023): 163–173.

67. P. Debnath, J. Sarkar, A. Talukdar, and S. Chatterjee, "Exploring the Potential of $CsPbI_3/CsPbBr_3$ Heterojunction as an Absorber Layer in Perovskite Solar Cells: A Numerical and Experimental Study," *Bulletin of Materials Science* 47, no. 3 (2024): 162.

68. L. M. Pazos-Outón, T. P. Xiao, and E. Yablonovitch, "Fundamental Efficiency Limit of Lead Iodide Perovskite Solar Cells," *The Journal of Physical Chemistry Letters* 9, no. 7 (2018): 1703–1711.

69. M. Liu, M. B. Johnston, and H. J. Snaith, "Efficient Planar Heterojunction Perovskite Solar Cells by Vapour Deposition," *Nature* 501, no. 7467 (2013): 395–398.

70. K. K. Maurya and V. N. Singh, "Sb_2Se_3/CZTS Dual Absorber Layer Based Solar Cell with 36.32% Efficiency: A Numerical Simulation," *Journal of Science: Advanced Materials and Devices* 7, no. 2 (2022): 100445.

71. S. Srivastava, A. K. Singh, P. Kumar, and B. Pradhan, "Comparative Performance Analysis of Lead-Free Perovskites Solar Cells by Numerical Simulation," *Journal of Applied Physics* 131, no. 17 (2022).

72. M. T. Islam, M. R. Jani, S. M. Al Amin, et al., "Numerical Simulation Studies of a Fully Inorganic $Cs_2AgBiBr_6$ Perovskite Solar Device," *Optical Materials* 105 (2020): 109957.

73. D. Pal and S. Das, "Defect and Interface Engineering of Highly Efficient La_2NiMnO_6 Planar Perovskite Solar Cell: A Theoretical Study," *Optical Materials* 108 (2020): 110453.